Supplementary information for:

A double-dysprosocenium single-molecule magnet bound together with neutral ligands

Peter Evans, Daniel Reta, Conrad A. P. Goodwin, Fabrizio Ortu, Nicholas F. Chilton and David P. Mills*

Department of Chemistry, School of Natural Sciences, The University of Manchester, Oxford Road, Manchester, M13 9PL, U.K.

Contents

1. Synthesis

General methods. All manipulations were conducted under argon with rigorous exclusion of oxygen and water using Schlenk line and glove box techniques. Pentane, diethyl ether, toluene, and THF were dried by passing through columns containing alumina; *n*-hexane and benzene were dried by refluxing over potassium and distillation; chlorobenzene was dried by refluxing over CaH_2 and distillation. Solvents were stored over potassium mirrors, except for THF and chlorobenzene, which were stored over 4 Å molecular sieves. All solvents were degassed before use. For NMR spectroscopy C_6D_5Cl was dried by refluxing over CaH_2 and vacuum transferred and degassed by three freeze-pump-thaw cycles before use. MeLi (1.6 M in diethyl ether), and $AlMe_3$ (2.0 M in hexanes) were purchased from Sigma-Aldrich and were used as received. $[Y(Cp^*)_2(\mu\text{-}Cl)_2K(THF)_2]$, $[Dy(Cp^*)_2(\mu\text{-}Cl)_2K(THF)_2]$, $[Y(Cp^*)_2(\mu\text{-}Me)_2Li]$ and $[\{Y(Cp^*)_2(\mu\text{-}Me_4Al)\}_2]$ were prepared according to literature methods[1] and were adapted here for Dy analogues; we include additional experimental details of these procedures for convenience. During the preparation of $[\{Y(Cp^*)_2(\mu\text{-}Me_4Al)\}_2]$ we obtained an improved single crystal XRD dataset over that previously reported,[1a] as well as a dataset for the precursor $[Y(Cp^*)_2(\mu\text{-}Me)_2Li(THF)]$; we have included these data herein. $[NEt_3H][Al\{OC(CF_3)_3\}_4]$[2] was also prepared by published procedures. ^1H (400 MHz), $^{13}C\{^1H\}$ (100 MHz and 125 MHz) and $^{19}F\{^1H\}$ (376 MHz) NMR spectra were obtained on an Avance III 400 MHz or 500 MHz spectrometer at 298 K. These were referenced to the solvent used, or to external TMS (^1H, ^{13}C) or $C_7H_5F_3/CDCl_3$ (^{19}F). ATR-Fourier Transform infrared (ATR-FTIR) spectra were recorded as microcrystalline powders using a Bruker Tensor 27 spectrometer. Elemental and ICP-OES analyses were performed by Mrs Anne Davies and Mr Martin Jennings at The University of Manchester School of Chemistry Microanalysis Service, Manchester, UK.

$[Y(Cp^*)_2(\mu\text{-}Me)_2Li]$. A solution of MeLi in Et_2O (1.6 M, 4.1 ml, 6.6 mmol) was added dropwise to a cold (–78 °C) solution of $[Y(Cp^*)_2(\mu\text{-}Cl)_2K(THF)_2]$ (1.9874 g, 3.24 mmol) in THF (50 mmol). The resultant pale yellow reaction mixture was allowed to warm slowly to room temperature overnight and volatiles were removed *in vacuo* to give a sticky yellow solid. The product was extracted into Et_2O (50 ml) and the pale yellow filtrate was reduced in volume to *ca*. 10 ml and was stored at –25 °C overnight

to give pale yellow microcrystalline material. This was isolated by decantation of the supernatant solution and was dried under vacuum to give putative "[Y(Cp*)$_2$(μ-Me)$_2$Li(THF)$_x$]." This material was desolvated by heating under vacuum (75 °C, 0.01 Torr) for 24 h to give [Y(Cp*)$_2$(μ-Me)$_2$Li] as a yellow powder. Yield: 1.0847 g, 84%. This material was used without further purification for the next step. On one occasion several crystals of [Y(Cp*)$_2$(μ-Me)$_2$Li(Et$_2$O)]were grown from a saturated diethyl ether solution at –25 °C overnight to confirm the identity of the intermediate by single crystal XRD.

[{Y(Cp*)$_2$(μ-Me$_4$Al)}$_2$]. A solution of AlMe$_3$ in hexanes (2.0 M, 3.2 ml, 6.4 mmol) was added to a suspension of [Y(Cp*)$_2$(Me)$_2$Li] (0.9973 g, 2.52 mmol) in toluene (30 ml) at room temperature. The resultant yellow reaction mixture with pale solids was stirred for 16 hours and allowed to settle. The reaction mixture was filtered and volatiles were removed *in vacuo* from the yellow filtrate to give a pale yellow solid. This was washed with pentane (10 ml) and dried under vacuum to give [{Y(Cp*)$_2$(μ-Me$_4$Al)}$_2$]. Yield: 0.1754 g, 16%. This material was used without further purification for the next step. On one occasion several crystals of [{Y(Cp*)$_2$(μ-Me$_4$Al)}$_2$]·(C$_7$H$_8$)$_2$ were grown from a saturated toluene solution at –25 °C overnight to confirm the identity of the product by single crystal XRD.

[Dy(Cp*)$_2$(μ-Me)$_2$Li]. A solution of MeLi in Et$_2$O (1.6 M, 3.3 ml, 5.3 mmol) was added dropwise to a pre-cooled (–78 °C) solution of [Dy(Cp*)$_2$(μ-Cl)$_2$K(THF)$_2$] (1.7912 g, 2.61 mmol) in THF (40 ml). The resultant yellow reaction mixture was allowed to warm to room temperature slowly overnight and the volatiles were removed *in vacuo* to give a tacky yellow solid. The product was extracted into diethyl ether (40 ml) and filtered. The yellow filtrate was reduced in volume to *ca*. 10 ml and was stored at –25 °C overnight to give "[Dy(Cp*)$_2$(μ-Me)$_2$Li(THF)$_x$]" as a yellow microcrystalline material. This was isolated by decantation of the supernatant solution and was desolvated by heating under vacuum (75 °C, 0.01 Torr) for 24 h to yield [Dy(Cp*)$_2$(μ-Me)$_2$Li] as a yellow powder. Yield: 0.9404 g, 77%. Anal. Calcd (%) for C$_{22}$H$_{36}$DyLi: C, 56.23; H, 7.72. Found: C, 53.77; H, 7.58. Low carbon values were reproducibly obtained for [Dy(Cp*)$_2$(μ-Me)$_2$Li]; this was attributed to incomplete combustion resulting from carbide formation. ^{1}H NMR (C$_6$D$_5$Cl, 400 MHz, 298 K): δ = –4.55 (br, *ν*½ = 200 Hz, 6H, Li(C*H*$_3$)$_2$, –16.06 (br, *ν*½ = 200 Hz, 30H, Cp-C*H*$_3$). The ^{13}C{^{1}H} NMR spectrum could not be interpreted due to

the paramagnetism of the sample. FTIR (ATR, microcrystalline): ῡ = 2960 (w, br), 2906 (w, br), 2859 (w, br), 1437 (w, br), 1385 (w), 1260 (w), 1137 (w), 1085 (w), 1021 (w, br), 945 (w, br), 798 (w), 589 (w), 512 (m), 485 (m) cm^{-1}.

[{Dy(Cp*)$_2$(μ-Me$_4$Al)}$_2$]. A solution of $AlMe_3$ in hexanes (2.0 M, 2.3 ml, 4.5 mmol) was added to a suspension of [Dy(Cp*)$_2$(μ-Me)$_2$Li] (0.8624 g, 1.84 mmol) in toluene (25 ml). The resulting yellow reaction mixture was filtered and the volatiles were removed *in vacuo*. The resultant solid was washed with pentane (10 ml) and dried *in vacuo* to give [{Dy(Cp*)$_2$(μ-Me$_4$Al)}$_2$] as a pale yellow powder. Yield: 0.1389 g, 15%. A small crop of crystals of [{Dy(Cp*)$_2$(μ-Me$_4$Al)}$_2$]·(C$_7$H$_8$)$_2$ were grown from a saturated toluene solution at –25 °C overnight to confirm the identity of the product by single crystal XRD. Anal. Calcd (%) for $C_{24}H_{42}AlDy$: C, 55.63; H, 8.14. Found: C, 55.42; H, 8.32. The ^1H and $^{13}C\{^1H\}$ NMR spectra could not be interpreted due to the paramagnetism of the sample. FTIR (ATR, microcrystalline): ῡ = 2911 (w, br), 2858 (w, br), 1437 (w), 1380 (w), 1175 (w), 1098 (w), 1020 (w), 901 (m), 777 (w), 739 (m), 672 (m), 620 (m), 566 (m), 542 (m) cm^{-1}.

[{Y(Cp*)$_2$(μ-Me$_3$AlNEt$_3$)}$_2$][Al{OC(CF$_3$)$_3$}$_4$]$_2$ (1-Y). [{Y(Cp*)$_2$(μ-Me$_4$Al)}$_2$] (0.1754 g, 0.20 mmol) and [NEt$_3$H][Al{OC(CF$_3$)$_3$}$_4$] (0.4200 g, 0.39 mmol) were suspended in benzene (15 ml); the reaction mixture was stirred overnight to give a colourless solution and crude **1-Y** as a pale yellow solid. The solvent was removed *in vacuo* and the product was extracted into chlorobenzene (15 ml) and filtered. The resultant pale yellow solution was reduced in volume to *ca*. 8 ml, layered with *n*-hexane (25 ml) and allowed to stand at room temperature overnight to afford off-white crystals of [{Y(Cp*)$_2$(μ-Me$_3$AlNEt$_3$)}$_2$][Al{OC(CF$_3$)$_3$}$_4$]$_2$·(C$_6$H$_5$Cl)$_3$ (**1-Y·3C$_6$H$_5$Cl**). The crystals were dried *in vacuo* to afford an off-white crystalline solid. Yield: 0.4933 g, 75%. Anal. Calcd (%) for $C_{108}H_{123}Al_4Cl_3F_{72}N_2O_8Y_2$: C, 38.87; H, 3.72; N, 0.84. Found: C, 36.43; H, 3.47; N, 0.78. Low carbon values were reproducibly obtained for **1-Y**; this was attributed to incomplete combustion resulting from carbide formation. ^1H NMR (C$_6$D$_5$Cl, 400 MHz, 298 K): δ = –0.74 (br m, 18H, Al(C*H*$_3$)$_3$), 0.95 (br m, 18H, N(CH$_2$C*H*$_3$)$_3$), 1.73 (s, 60H, C$_5$(CH$_3$)$_5$), 2.52 (br m, 12H, N(C*H*$_2$CH$_3$)$_3$). A second species was identified in solution that arises from dynamic equilibria but this is not included in the assignment of the spectrum here.

$^{13}C\{^1H\}$ NMR (C_6D_5Cl, 100 MHz, 298 K): δ = 8.75, 9.00 ($N(CH_2\mathit{C}H_3)_3$), 10.98, 11.26 ($C_5(\mathit{C}H_3)_5$), 47.99 ($N(\mathit{C}H_2CH_3)_3$), 120.82, 122.86, 123.18 ($\mathit{C}_5(CH_3)_5$). Multiple signals arise from dynamic equilibria; $Al(\mathit{C}H_3)_3$ not observed due to quadrupolar broadening by I = 5/2 ^{27}Al nuclei and additional splitting by I = 1/2 ^{88}Y nuclei. $^{19}F\{^1H\}$ NMR (C_6D_5Cl, 376 MHz, 298 K): δ = –74.66. FTIR (ATR, microcrystalline): ῡ = 2915 (w, br), 1455 (w), 1398 (w), 1352 (w), 1297 (m), 1273 (m), 1239 (m), 1209 (s), 1163 (m), 1086 (w), 1043 (w), 969 (s), 895 (m), 831 (w), 795 (w, br), 755 (w), 744 (w), 726 (s), 688 (w), 688 (w), 560 (m), 536 (m), 442 (m) cm^{-1}.

$[\{Dy(Cp^*)_2(\mu\text{-}Me_3AlNEt_3)\}_2][Al\{OC(CF_3)_3\}_4]_2$ (1-Dy). A slurry of $[\{Dy(Cp^*)_2(\mu\text{-}Me_4Al)\}_2]$ (0.1389 g, 0.13 mmol) and $[NEt_3H][Al\{OC(CF_3)_3\}_4]$ (0.2855 g, 0.27 mmol) were suspended in benzene (10 ml); the reaction mixture was stirred overnight to give a colourless solution and crude **1-Dy** as a pale yellow solid. The solvent was removed *in vacuo* and the product was extracted into chlorobenzene (15 ml) and filtered. The resultant pale yellow solution was reduced in volume to *ca*. 5 ml, layered with *n*-hexane (20 ml) and allowed to stand at room temperature overnight to afford yellow crystals of $[\{Dy(Cp^*)_2(\mu\text{-}Me_3AlNEt_3)\}_2][Al\{OC(CF_3)_3\}_4]_2\cdot(C_6H_5Cl)_3$ (**1-Dy·3C_6H_5Cl**). The crystals were dried *in vacuo* to afford a yellow crystalline solid, which elemental analysis results indicate is desolvated **1-Dy**. Yield: 0.3606 g, 76%. Anal. Calcd (%) for $C_{108}H_{123}Al_4Cl_3F_{72}N_2O_8Dy_2$: C, 37.23; H, 3.56; N, 0.80. Found: C, 34.53; H, 3.38; N, 0.14. Low carbon values were reproducibly obtained for **1-Dy**; this was attributed to incomplete combustion resulting from carbide formation, whilst the low nitrogen value is a consequence of the experimental limitations of the apparatus for the accurate measurement of nitrogen values < 1%. $^{19}F\{^1H\}$ NMR (C_6D_5Cl, 376 MHz, 298 K): δ = –81.40 (br, ν½ = 140 Hz), –80.28 (br, ν½ = 400 Hz); the presence of two signals is attributed to dynamic equilibrium processes in solution. The ^1H and $^{13}C\{^1H\}$ NMR spectra could not be interpreted due to the paramagnetism of the sample. FTIR (ATR, microcrystalline): ῡ = 2921 (w, br), 1453 (w), 1398 (w), 1352 (w), 1297 (m), 1274 (m), 1239 (m), 1209 (st), 1162 (m), 1087 (w), 1045 (w), 1022 (w), 969 (st), 830 (w), 805 (w), 789 (w), 755 (w), 742 (w), 726 (st), 689 (w), 653 (w), 560 (w), 536 (m), 440 (m) cm^{-1}.

[{0.05Dy@0.95Y(Cp*)$_2$(μ-Me$_3$AlNEt$_3$)}$_2$][Al{OC(CF$_3$)$_3$}$_4$]$_2$ (1-Dy@Y). A mixture of **1-Y** (0.2643 g, 0.079 mmol) and **1-Dy** (0.0146 g, 0.0042 mmol) was dissolved in chlorobenzene (5 ml), layered with *n*-hexane (15 ml) and allowed to stand at room temperature overnight to afford off-white crystals of [{0.05Dy@0.95Y(Cp*)$_2$(μ-Me$_3$AlNEt$_3$)}$_2$][Al{OC(CF$_3$)$_3$}$_4$]$_2$·(C$_6$H$_5$Cl)$_3$ (**1-Dy@Y·3C$_6$H$_5$Cl**). The crystals were dried *in vacuo* to afford an off-white crystalline solid. Yield (0.2340 g, 84%). $C_{108}H_{123}Al_4Cl_3F_{72}N_2O_8Dy_{0.1}Y_{1.9}$: C, 38.79; H, 3.71; N, 0.84. Found: C, 34.51; H, 3.19; N, 0.0. Low carbon values were reproducibly obtained for **1-Dy@Y**; this was attributed to incomplete combustion resulting from carbide formation, whilst the low nitrogen value is a consequence of the experimental limitations of the apparatus for the accurate measurement of nitrogen values < 1%. Y/Dy composition (ICP-OES): Y, 94.6; Dy, 5.4. FTIR (ATR, microcrystalline): ῡ = 2916 (w, br), 1478 (w), 1454 (w), 1398 (w), 1352 (w), 1297 (m), 1273 (m), 1239 (m), 1208 (st), 1161 (m), 1085 (w), 1043 (w), 1023 (w), 969 (st), 831 (w), 793 (w, br), 754 (w), 725 (st), 688 (w), 653 (w), 560 (m), 536 (w), 441 (m) cm^{-1}.

[{0.05Dy@0.95Y(Cp*)$_2$(μ-Me$_3$AlNEt$_3$)}$_2$][Al{OC(CF$_3$)$_3$}$_4$]$_2$ (1-Dy@Y_2). A mixture of [{Y(Cp*)$_2$(μ-Me$_4$Al)}$_2$] (0.1661 g, 0.19 mmol), [{Dy(Cp*)$_2$(μ-Me$_4$Al)}$_2$] (0.0102 g, 0.01 mmol) and [NEt$_3$H][Al{OC(CF$_3$)$_3$}$_4$] (0.4186 g, 0.392 mmol) were suspended in benzene (15 ml); the reaction mixture was stirred overnight to give a colourless solution and crude **1-Dy@Y_2** as a pale yellow solid. The volatiles were removed *in vacuo* and the product was extracted in chlorobenzene (10 ml) and filtered. The resultant yellow solution was reduced in volume to *ca*. 5 ml, layered with *n*-hexane (20 ml) and allowed to stand at room temperature overnight to afford off-white crystals of [{0.05Dy@0.95Y(Cp*)$_2$(μ-Me$_3$AlNEt$_3$)}$_2$][Al{OC(CF$_3$)$_3$}$_4$]$_2$·(C$_6$H$_5$Cl)$_3$ (**1-Dy@Y_2·3C$_6$H$_5$Cl**). The crystals were dried *in vacuo* to afford an off-white crystalline solid. Yield (0.5268 g, 80%).

2. Crystallography

The crystal data for [Y(Cp*)$_2$(μ-Me)$_2$Li(THF)], [{Ln(Cp*)$_2$(μ-Me$_4$Al)}$_2$]·(C$_7$H$_8$)$_2$ (Ln = Dy, Y) and **1-Ln·3C$_6$H$_5$Cl** (Ln = Dy, Y, 0.05Dy@0.95Y) are compiled in Tables S1-S2. Crystals were examined using a Rigaku XtalLAB AFC11 diffractometer equipped with a CCD area detector and graphite-monochromated Cu Kα (λ = 1.54178 Å) or Mo Kα radiation (λ = 0.71073 Å), apart from [Y(Cp*)$_2$(μ-Me)$_2$Li(THF)], which was examined using an Oxford Diffraction Supernova diffractometer equipped with a CCD area detector and mirror-monochromated Mo Kα radiation (λ = 0.71073 Å). Intensities were integrated from data recorded on 1° ([Y(Cp*)$_2$(μ-Me)$_2$Li(THF)]) **1-Ln·3C$_6$H$_5$Cl** (Ln = Y, 0.05Dy@0.95Y) or 0.5° (**1-Dy·3C$_6$H$_5$Cl**, [{Ln(Cp*)$_2$(μ-Me$_4$Al)}$_2$]·(C$_7$H$_8$)$_2$) frames by ω rotation. Cell parameters were refined from the observed positions of all strong reflections in each data set. A Gaussian grid face-indexed ([Y(Cp*)$_2$(μ-Me)$_2$Li(THF)], **1-Ln·3C$_6$H$_5$Cl**) or multi-scan ([{Ln(Cp*)$_2$(μ-Me$_4$Al)}$_2$]·(C$_7$H$_8$)$_2$) absorption correction with a beam profile was applied.[3] The structures were solved using SHELXS;[4] the datasets were refined by full-matrix least-squares on all unique F^2 values,[5] with anisotropic displacement parameters for all non-hydrogen atoms, and with constrained riding hydrogen geometries; U_{iso}(H) was set at 1.2 (1.5 for methyl groups) times U_{eq} of the parent atom. The largest features in final difference syntheses were close to heavy atoms and were of no chemical significance. CrysAlisPro[3] was used for control and integration, and SHELX[4,5] was employed through OLEX2[6] for structure solution and refinement. ORTEP-3[7] and POV-Ray[8] were employed for molecular graphics. The position of the H atoms belonging to the methyl groups involved in Ln···C interactions have been clearly identified in the difference maps for **1-Y** (C21 and C23) and [{Y(Cp*)$_2$(μ-Me$_4$Al)}$_2$] (C21 and C22); the H position assignment is also satisfactory for the analogous **1-Dy** and [{Dy(Cp*)$_2$(μ-Me$_4$Al)}$_2$], though such positions are not as well resolved in the difference maps, as expected because of the proximity of heavier metal centres (see Figures S5 and S6). CCDC 1964114–1964119 contain the supplementary crystal data for this article. These data can be obtained free of charge from the Cambridge Crystallographic Data Centre via www.ccdc.cam.ac.uk/data_request/cif.

Table S1. Crystallographic data for [Y(Cp*)$_2$(μ-Me)$_2$Li(THF)] and [{Ln(Cp*)$_2$(μ-Me$_4$Al)}$_2$]·(C$_7$H$_8$)$_2$ (Ln = Dy, Y).

[a]Conventional $R = \Sigma||Fo| - |Fc||/\Sigma|Fo|$; $Rw = [\Sigma w(Fo^2 - Fc^2)^2/\Sigma w(Fo^2)^2]^{1/2}$; $S = [\Sigma w(Fo^2 - Fc^2)^2/\text{no. data} - \text{no. params})]^{1/2}$ for all data.

	[Y(Cp*)$_2$(μ-Me)$_2$Li(THF)]	[{Dy(Cp*)$_2$(μ-Me$_4$Al)}$_2$]·(C$_7$H$_8$)$_2$	[{Y(Cp*)$_2$(μ-Me$_4$Al)}$_2$]·(C$_7$H$_8$)$_2$
Formula	$C_{26}H_{44}LiOY$	$C_{76}H_{116}Al_2Dy_2$	$C_{76}H_{116}Al_2Y_2$
Formula weight	468.46	1408.64	1261.46
Crystal size, mm	0.17 × 0.11 × 0.08	0.242 × 0.119 × 0.059	0.471 × 0.373 × 0.339
Crystal system	monoclinic	Triclinic	triclinic
Space group	$P2_1/n$	P-1	P-1
a, Å	9.2530(13)	11.1938(3)	11.2354(3)
b, Å	15.4572(12)	12.4457(7)	12.4540(3)
c, Å	18.378(2)	14.8073(5)	14.8193(2)
α, °	90	104.044(4)	103.894(2)
β, °	94.016(10)	100.205(3)	100.299(2)
γ, °	90	111.785(4)	111.860(2)
V, Å^3	2621.9(5)	1774.66(15)	1783.50(8)
Z	4	1	1
Temperature, K	150	100	100
ρ_{calc}, g cm^3	1.187	1.318	1.174
μ, mm^{-1}	2.237	2.153	2.688
F(*000*)	1000	730	676
No. of reflections (unique)	4797 (2680)	25170 (11216)	24477 (6466)
S[a]	0.99	1.04	1.14
$R_1(wR_2)$ ($F^2 > 2\sigma(F^2)$)	0.0954 (0.1760)	0.0941 (0.2574)	0.0444 (0.1278)
R_{int}	0.141	0.046	0.034
Min./max. diff map, Å^{-3}	−0.63, 0.56	−2.38, 1.61	−0.58, 1.85

Table S2. Crystallographic data for **1-Ln·3C$_6$H$_5$Cl** (Ln = Dy, Y, 0.05Dy@0.95Y).

[a]Conventional $R = \Sigma||Fo| - |Fc||/\Sigma|Fo|$; $Rw = [\Sigma w(Fo^2 - Fc^2)^2/\Sigma w(Fo^2)^2]^{1/2}$; $S = [\Sigma w(Fo^2 - Fc^2)^2/\text{no. data} - \text{no. params})]^{1/2}$ for all data.

	1-Dy·3C$_6$H$_5$Cl	**1-Y·3C$_6$H$_5$Cl**	**1-Dy@Y·3C$_6$H$_5$Cl**
Formula	$C_{108}H_{123}Al_4Cl_3Dy_2F_{72}N_2O_8$	$C_{109}H_{124}Al_4Cl_3F_{72}N_2O_8Y_2$	$C_{108}H_{123}Al_4Cl_3Dy_{0.22}F_{72}N_2O_8Y_{1.78}$
Formula weight	3484.35	3350.18	3353.36
Crystal size, mm	0.175 × 0.096 × 0.079	0.160 × 0.116 × 0.060	0.218 × 0.169 × 0.074
Crystal system	Monoclinic	Monoclinic	monoclinic
Space group	$P2_1/c$	$P2_1/c$	$P2_1/c$
a, Å	13.8684(3)	100.02(10)	14.14639(9)
b, Å	30.4814(7)	14.1215(2)	30.4739(2)
c, Å	16.1283(5)	30.3026(3)	16.04187(10)
α, °	90	16.0232(2)	90
β, °	97.720(3)	90	98.2178(6)
γ, °	90	98.4210(10)	90
V, Å^3	6756.1(3)	90	6844.58(8)
Z	2	6782.70(15)	2
Temperature, K	100	100	150
ρ_{calc}, g cm^3	1.713	2	1.627
μ, mm^{-1}	8.035	1.640	3.801
F(*000*)	3464	3370	3368
No. of reflections (unique)	43524 (13559)	39902 (13772)	41213 (13952)
S[a]	1.15	1.01	1.05
$R_1(wR_2)$ ($F^2 > 2\sigma(F^2)$)	0.0720 (0.2050)	0.0783 (0.2319)	0.0452 (0.1251)
R_{int}	0.076	0.027	0.022
Min./max. diff map, Å^{-3}	−2.00, 1.12	−0.84, 1.13	−0.57, 1.13

3. Molecular structures

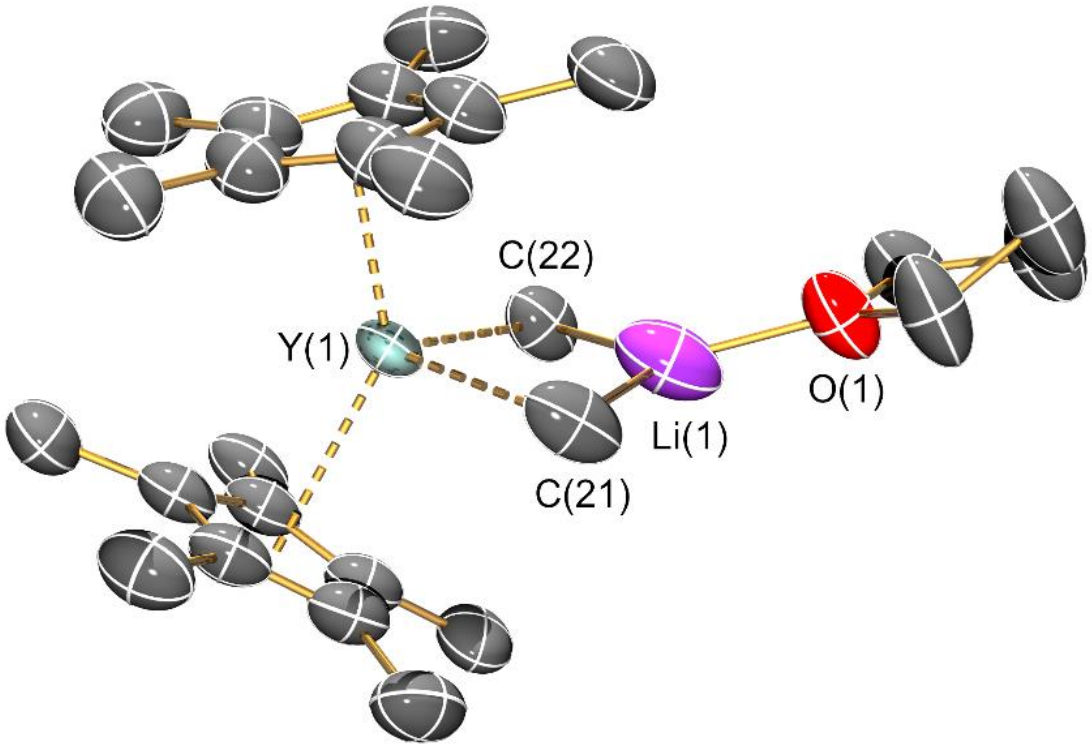

Figure S1. Molecular structure of $[Y(Cp^*)_2(\mu\text{-}Me)_2Li(THF)]$. Displacement ellipsoids set at 50 % probability level; disorder components (Cp* and THF) and hydrogen atoms are omitted for clarity. Selected bond lengths (Å) and angles (°): Y(1)···$Cp_{centroid}1$: 2.37(2); Y(1)···$Cp_{centroid}2$: 2.45(2); Y(1)–C(21): 2.505(10); Y(1)–C(22): 2.500(10); Li(1)–C(21): 2.13(2); Li(1)–C(22): 2.13(2); Y(1)–O(1): 1.84(2); range Y(1)–C_{ring}: 2.62(3)–2.69(2); $Cp_{centroid}1$···Y(1)···$Cp_{centroid}2$: 141.1(3); C(21)–Y(1)–C(22): 90.8(3); Y(1)–C(21)–Li(1): 77.2(7); Y(1)–C(22)–Li(1): 77.3(7); C(21)–Li(1)–C(22): 113.5(12).

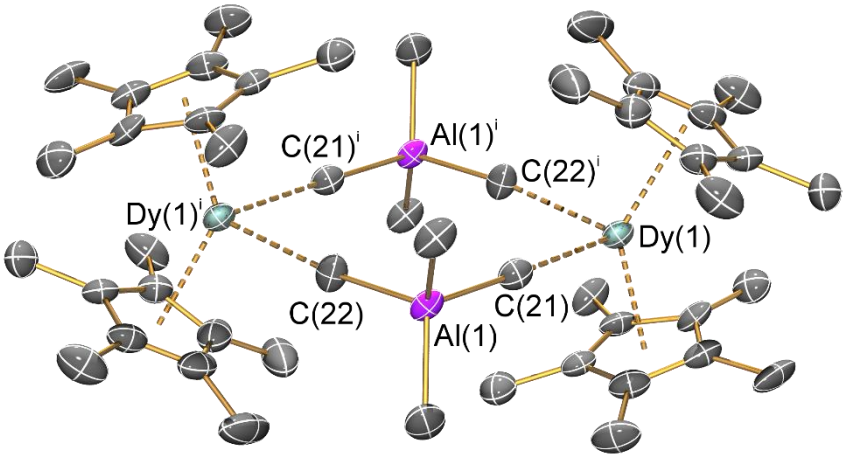

Figure S2. Molecular structure of $[\{Dy(Cp^*)_2(\mu\text{-}Me_4Al)\}_2]\cdot(C_7H_8)_2$. Displacement ellipsoids set at 50 % probability level and hydrogen atoms and lattice solvent are omitted for clarity. Symmetry operation to generate equivalent atoms: i = *–x*, *–y*, *–z*. Selected bond lengths (Å) and angles (°): Dy(1)···$Cp_{centroid}$1: 2.355(7); Dy(1)···$Cp_{centroid}$2: 2.372(7); Dy(1)···C(21): 2.68(2); Dy(1)···C(22): 2.70(2); Al(1)–C(21): 2.04(2); Al(1)–C(22): 2.05(2); range Dy(1)–C_{ring}: 2.63(2)–2.67(2); $Cp_{centroid}$1···Dy(1)···$Cp_{centroid}$2: 138.7(2); C(21)···Dy(1)···C(22): 87.2(2); Dy(1)···C(21)···Al(1): 175.6(8); C(21)···Al(1)···C(22): 100.7(7); Dy(1)···C(21)–Al(1): 175.6(8).

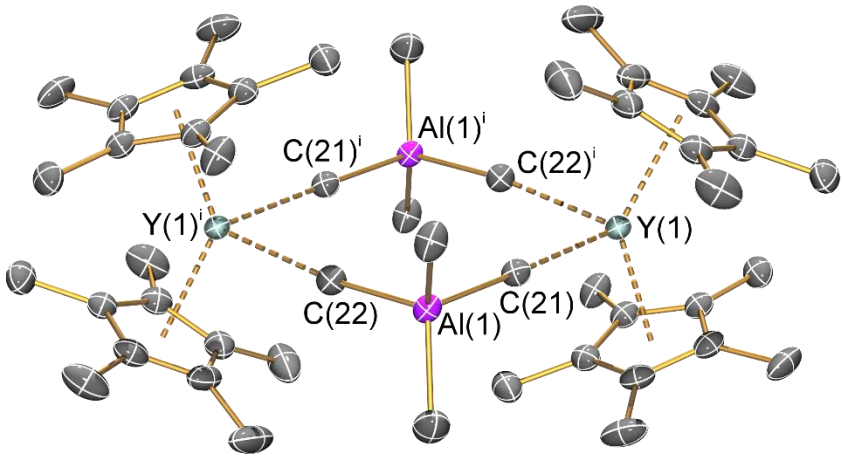

Figure S3. Molecular structure of $[\{Y(Cp^*)_2(\mu\text{-}Me_4Al)\}_2]\cdot(C_7H_8)_2$. Displacement ellipsoids set at 50 % probability level and hydrogen atoms and lattice solvent are omitted for clarity. Symmetry operation to generate equivalent atoms: i = *–x*, *–y*, *–z*. Selected bond lengths (Å) and angles (°): Y(1)···$Cp_{centroid}1$: 2.351(2); Y(1)···$Cp_{centroid}2$: 2.365(2); Y(1)···C(21): 2.669(4); Y(1)···C(22): 2.686(3); Al(1)–C(21): 2.039(3); Al(1)–C(22): 2.049(3); range Y(1)–C_{ring}: 2.627(3)–2.675(4); $Cp_{centroid}1$···Y(1)···$Cp_{centroid}2$: 138.65(5); C(21)···Y(1)···C(22): 87.39(10); Y(1)···C(21)···Al(1): 175.5(2); C(21)···Al(1)···C(22): 100.4(2); Y(1)···C(21)–Al(1): 175.5(2).

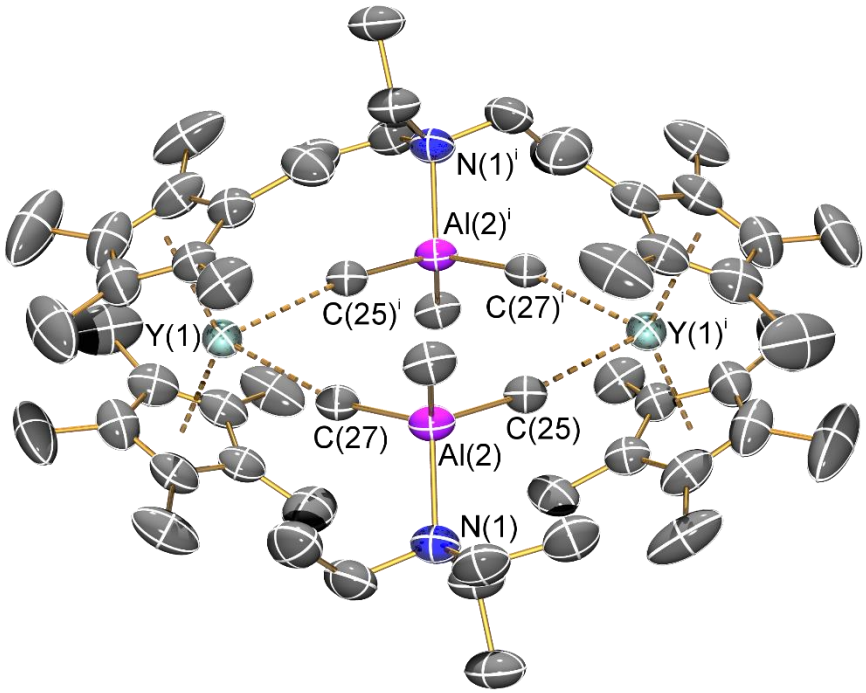

Figure S4. Molecular structure of the dication of **1-Y·3C$_6$H$_5$Cl**, shown at the 50 % probability level; [Al{OC(CF$_3$)$_3$}$_4$]$^-$ counterions and lattice solvent are omitted for clarity. Symmetry operation to generate equivalent atoms: i = 1–*x*, 1–*y*, 1–*z*. Selected bond lengths (Å) and angles (°): Y(1)···Cp$_{centroid}$1: 2.339(2); Y(1)···Cp$_{centroid}$2: 2.360(3); Y(1)···C(25): 2.776(5); Y(1)···C(27): 2.782(5); range Y(1)–C$_{ring}$: 2.55(2)–2.65(3); Cp$_{centroid}$1···Y(1)···Cp$_{centroid}$2: 137.99(10); Cp$_{centroid}$1···Y(1)···C(25): 108.43(11); Cp$_{centroid}$1···Y(1)···C(27): 107.19(11); Cp$_{centroid}$2···Y(1)···C(25): 102.55(11); Cp$_{centroid}$2···Y(1)···C(25): 104.08(11); C(21)···Y(1)···C(27): 83.01(13) Y(1)···C(25)–Al(2): 175.6(8).

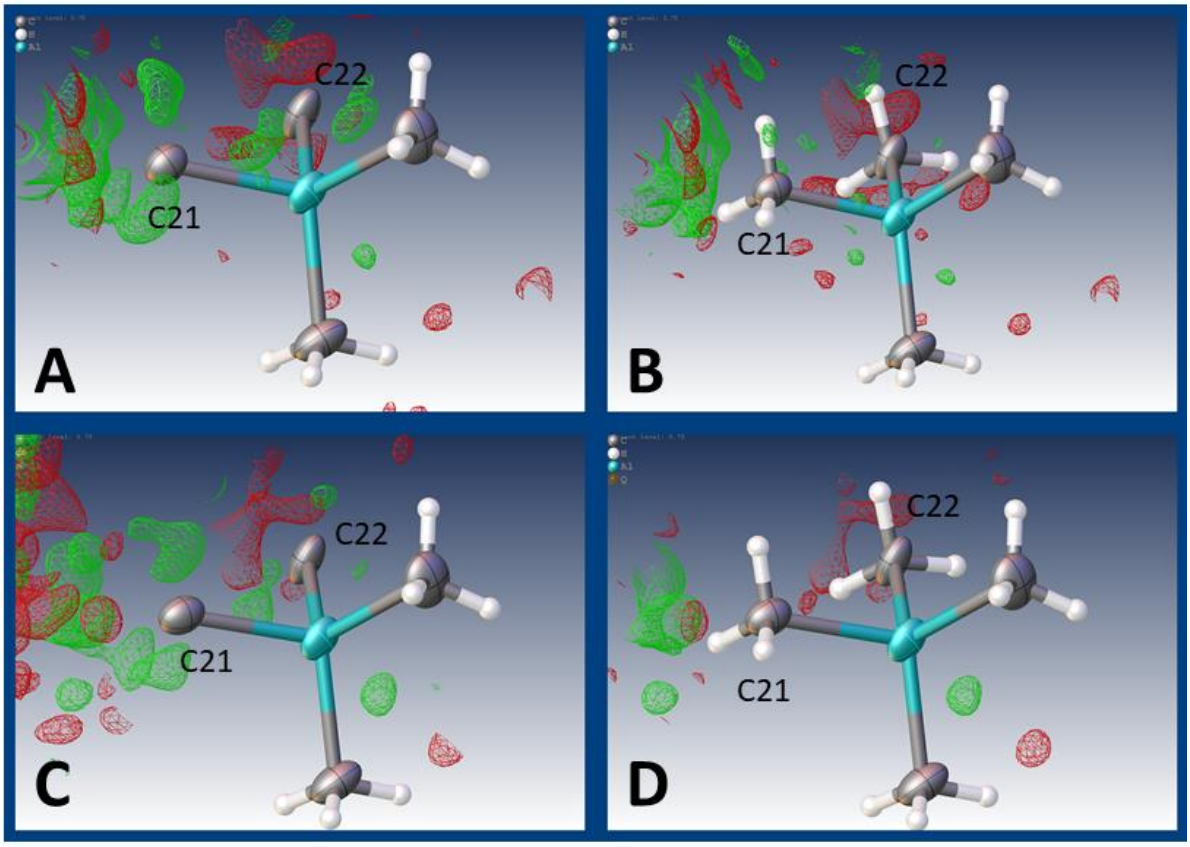

Figure S5. Difference maps (0.75 eÅ^{-3}) focused around the $\{AlMe_4\}^-$ unit of $[\{Dy(Cp^*)_2(\mu\text{-}Me_4Al)\}_2]\cdot(C_7H_8)_2$. Top: ShelXL refinement before (left, **A**) and after (right, **B**) addition of hydrogen atoms to C21 and C22; bottom: Olex2 refinement before (left, **C**) and after (right, **D**) addition of hydrogen atoms to C21 and C22. The Olex2 refinement includes anharmonic refinement of Dy1, which leads to an overall improvement of the difference map. More specifically, whilst the H position around C21 was somewhat defined with ShelXL treatment, density around atom C22 was poorly resolved (**A**); Olex2 refinement (with selective anharmonic treatment) sharpened the local difference map and allowed clear identification of the positions of the H atoms around C22 (**C**).

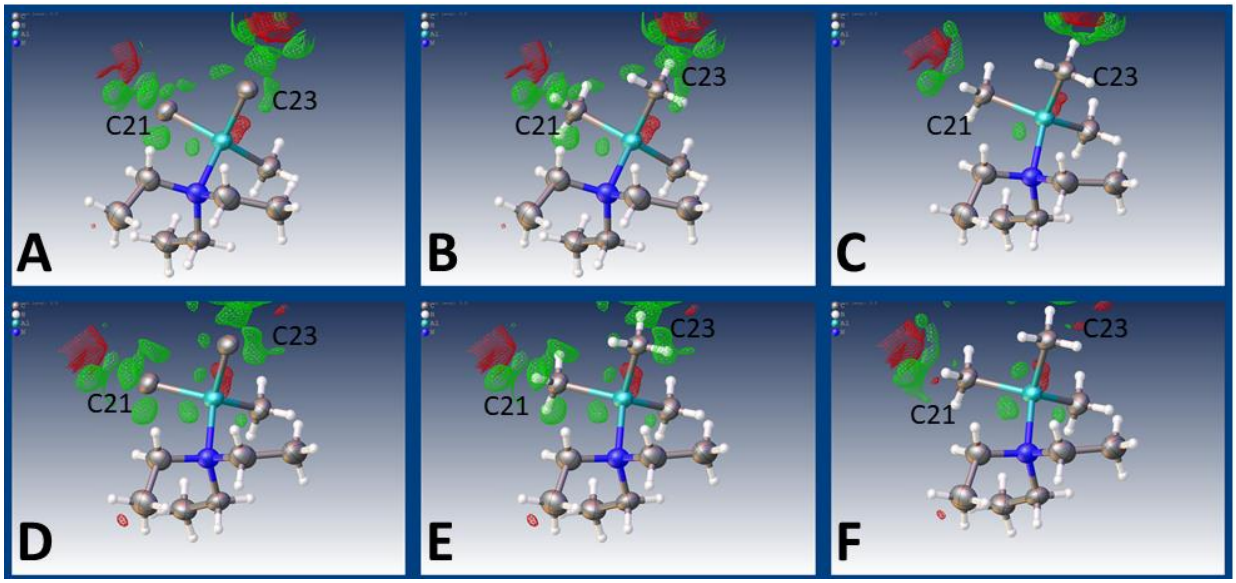

Figure S6. Difference maps (0.5 eÅ^{-3}) focused around the Me_3AlNEt_3 unit of **1-Dy**. Top: ShelXL refinement before (left, **A**) and after (right, **C**) addition of hydrogen atoms to C21 and C23; bottom: Olex2 refinement before (left, **D**) and after (right, **E**) addition of hydrogen atoms to C21 and C23. Pictures **B** and **D** show the positioning of the hydrogen atoms of C21 and C23 (HADD -r) with respect to the difference map prior to refinement. In this case ShelXL treatment affords a better final result, with a better resolution of the H positions around atoms C21 and C23 (**A** and **D**). Olex2 refinement includes anharmonic refinement of Dy1, but does not leads to an overall improvement of the difference map around both carbon atoms.

4. NMR spectroscopy

The initial ^{1}H NMR spectrum of **1-Y** contained the four resonances expected for the {Y(Cp*)$_2$(Me$_3$AlNEt$_3$)} moieties, together with additional resonances for NEt$_3$ and Cp* protons. We interpret these data to propose that **1-Ln** rapidly establish a monomer-dimer equilibrium in C_6D_5Cl solution; this mixture is then subject to various ligand scrambling and decomposition processes promoted by C_6D_5Cl to give a complex mixture of products. By analysis of NEt$_3$ integrals in the initial ^{1}H NMR spectrum of **1-Y** we establish an initial dimer : monomer ratio of approximately 2 : 1, with the broadest signals attributed to the dimeric species. Four of the five expected resonances were observed in the ^{13}C{^{1}H} NMR spectrum of **1-Y**, with the AlMe$_3$ groups not observed due to a combination of the poor solubility of the complex in C_6D_5Cl, quadrupolar broadening by I = 5/2 ^{27}Al nuclei and additional splitting by I = 1/2 ^{88}Y nuclei. The ^{19}F{^{1}H} NMR spectrum of **1-Y** exhibits a single resonance at –74.66 ppm; we tentatively attribute the differences between the ^{19}F NMR spectra of **1-Y** and **1-Dy** to paramagnetic shifts distinguishing the ^{19}F nuclei of anions associated with monomers and dimers.

To investigate if coordinating solvents coordinate to **1-Ln** to displace the {Me$_3$AlNEt$_3$} moieties we added diethyl ether to a sample of **1-Y** in a Youngs tap-appended NMR tube. The sample effervesced to give a pale yellow solution. We removed volatiles *in vacuo*, dissolved the resultant tacky solid in C_6D_5Cl, and acquired a ^{1}H NMR spectrum within 15 minutes (Figure S14). The presence of >2 eq. of diethyl ether in this sample indicates that this has coordinated to the Y^{3+} centre, presumably displacing {Me$_3$AlNEt$_3$}. As diethyl ether is less polar, less coordinating and less prone to decomposition pathways in the presence of Lewis acidic metal cations than THF, we did not add THF or other polar solvents to **1-Y**. Given that the equatorial interactions of Lewis bases to Dy^{3+} centres reduce the axiality of the resultant complex and promote magnetic relaxation pathways, which we were keen to avoid for favourable SMM properties, we did not investigate **1-Ln** in coordinating solvents further and all other NMR spectra were obtained in C_6D_5Cl.

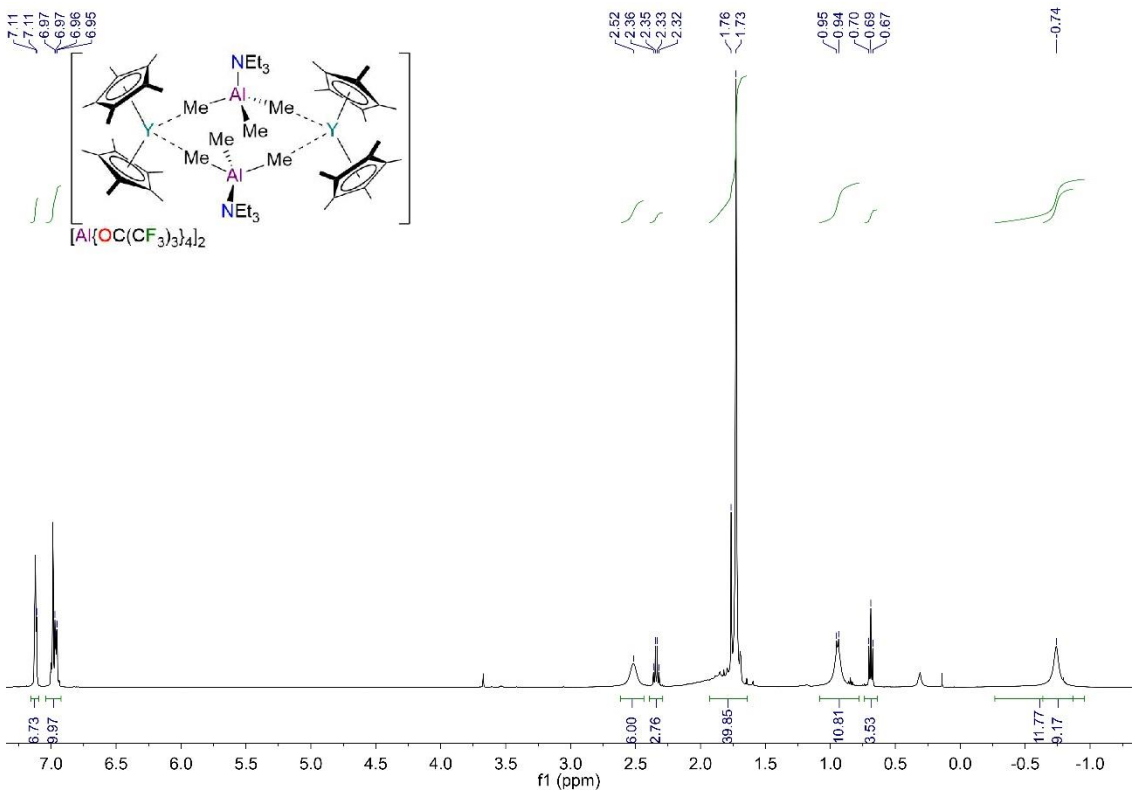

Figure S7. Initial ^{1}H NMR spectrum of **1-Y** in C_6D_5Cl.

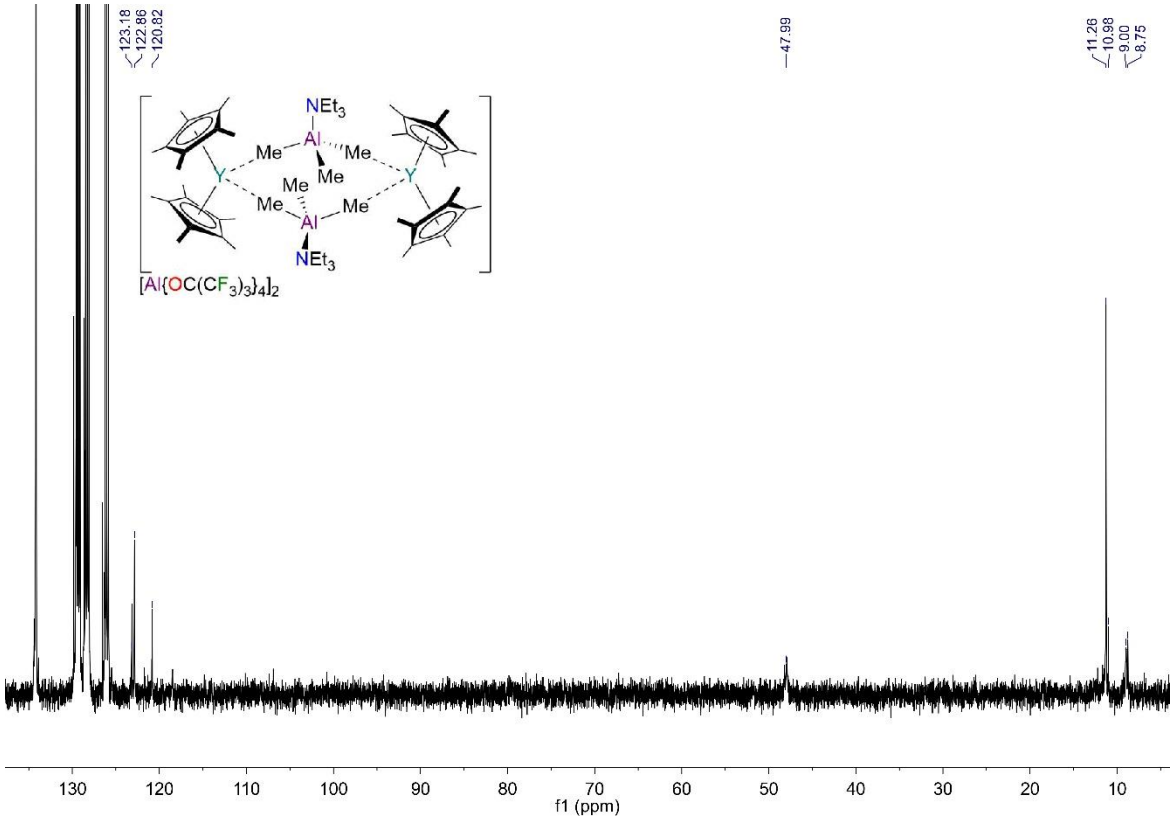

Figure S8. Initial $^{13}C\{^{1}H\}$ NMR spectrum of **1-Y** in C_6D_5Cl.

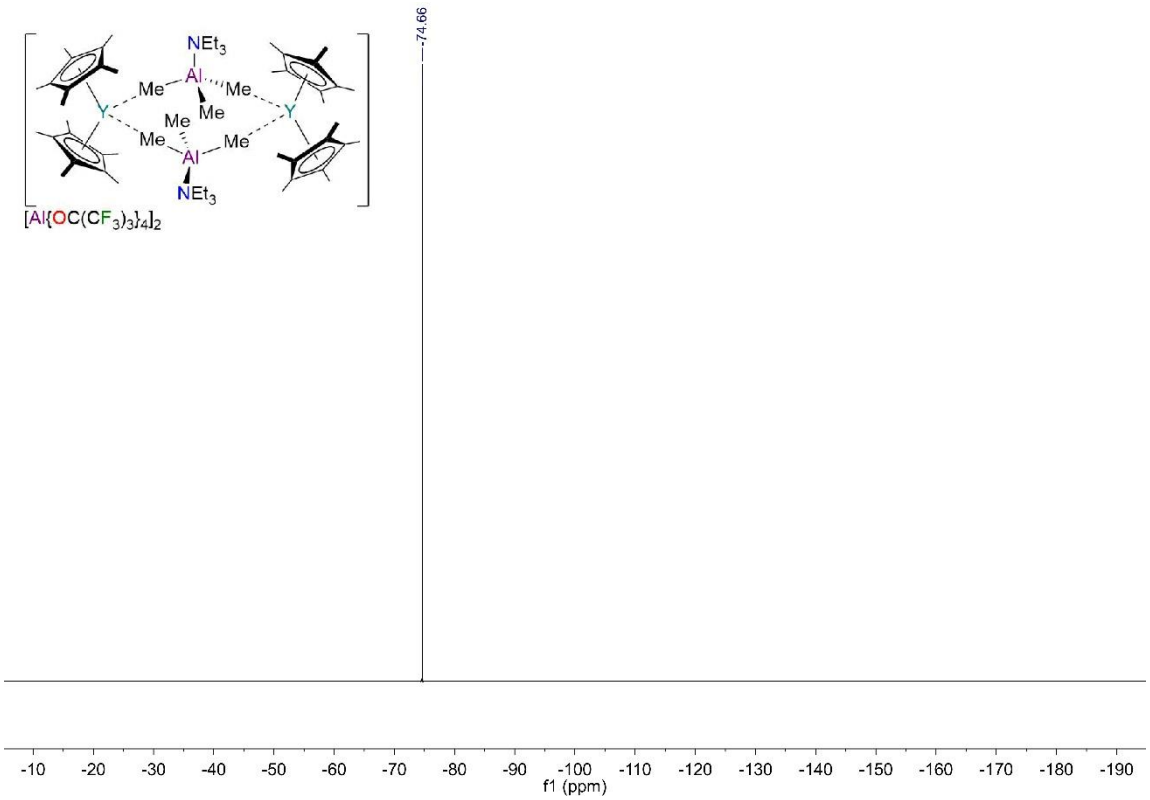

Figure S9. Initial $^{19}F\{^{1}H\}$ NMR spectrum of **1-Y** in C_6D_5Cl.

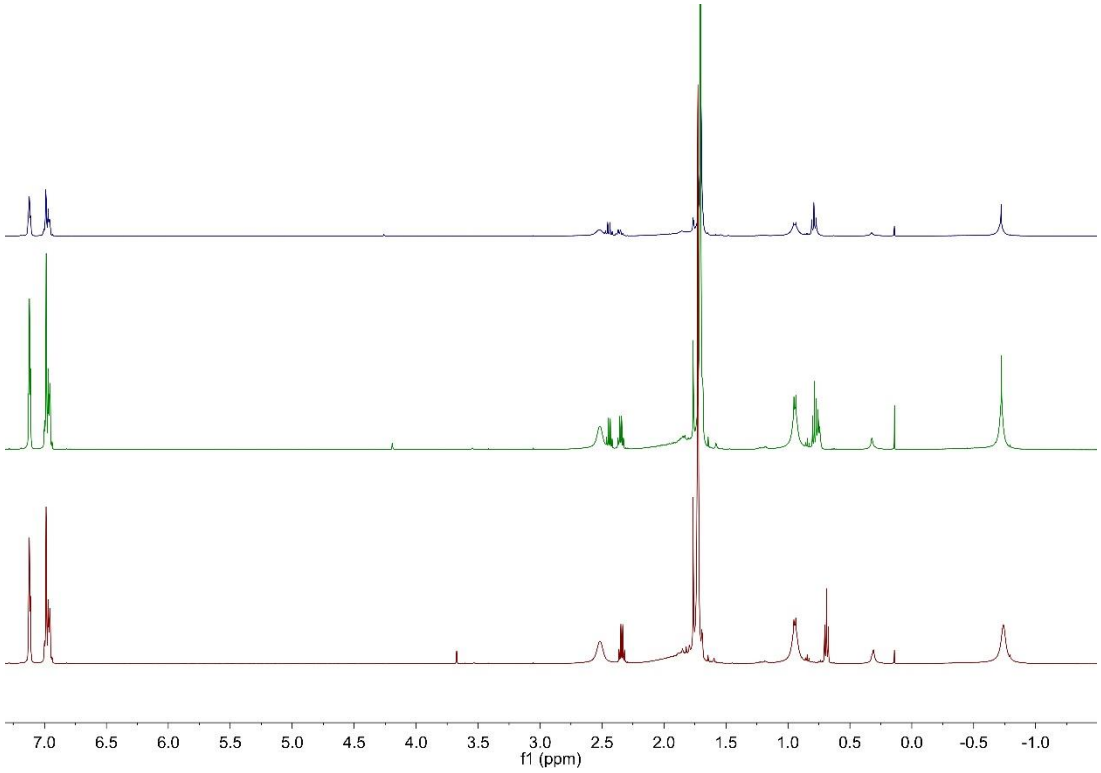

Figure S10. ^{1}H NMR spectra of **1-Y** in C_6D_5Cl to show decomposition of the sample over time at room temperature (bottom 10 mins, middle 5 hrs, top 22 hrs).

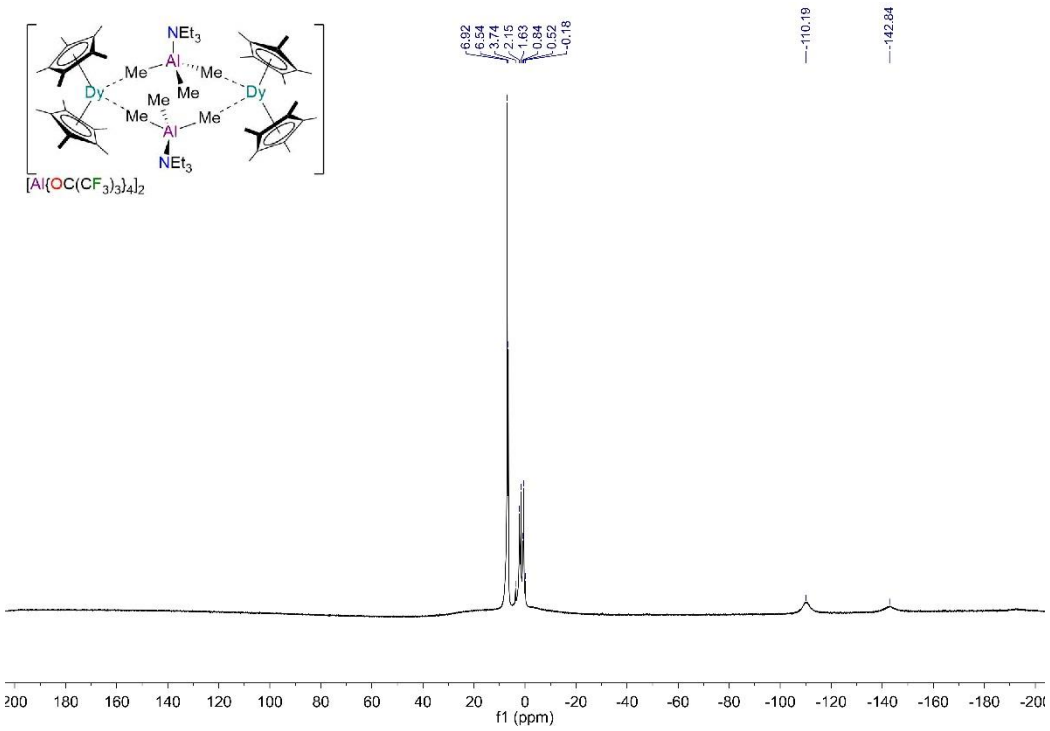

Figure S11. Initial ^{1}H NMR spectrum of **1-Dy** in C_6D_5Cl, zoomed in the region +200 to –200 ppm; no other signals were observed between +400 to –400 ppm. The signals between 0 to +10 ppm are assigned to C_6D_5Cl.

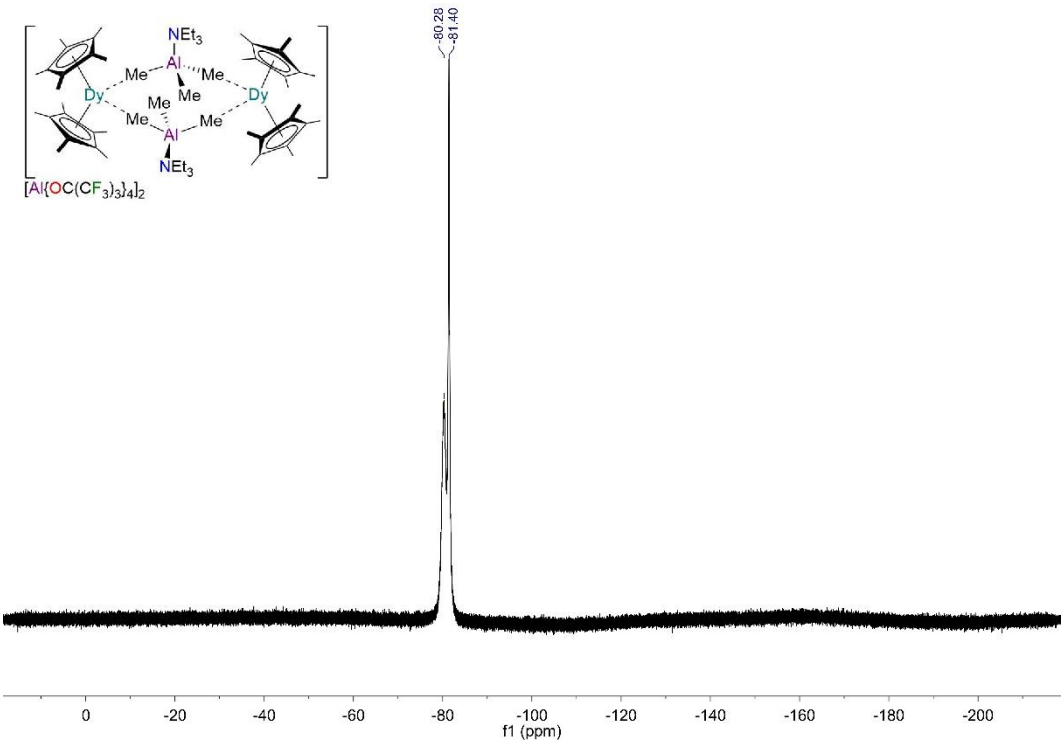

Figure S12. Initial $^{19}F\{^{1}H\}$ NMR spectrum of **1-Dy** in C_6D_5Cl.

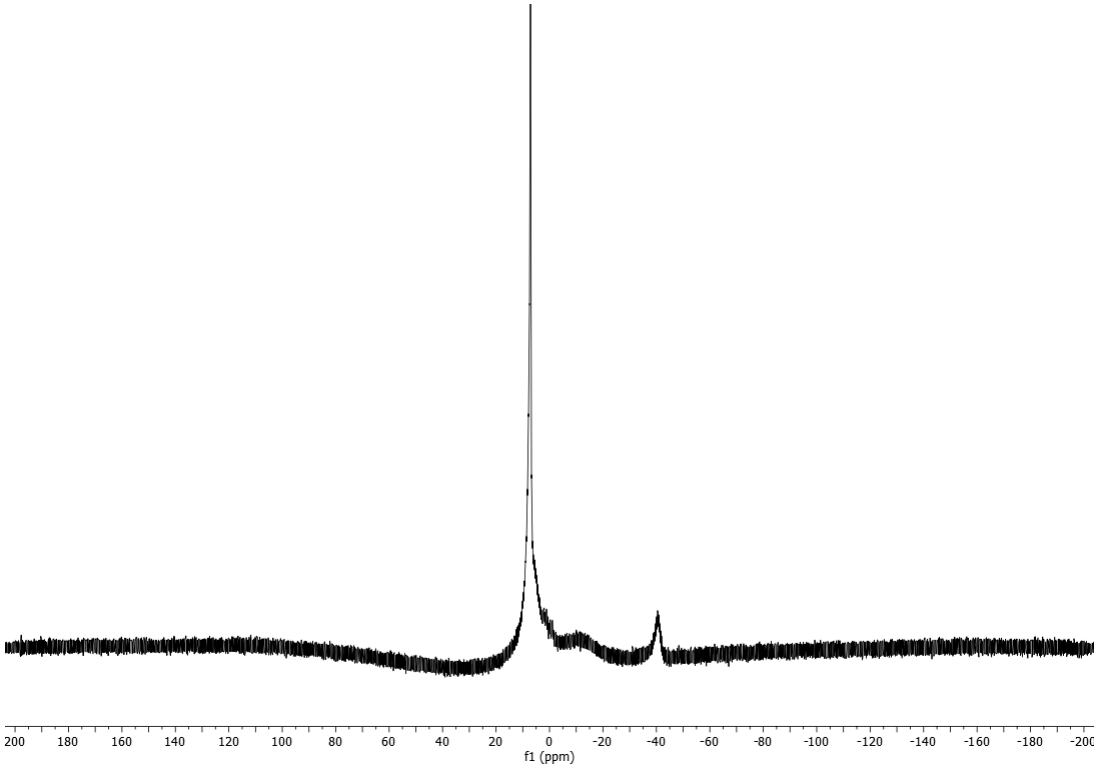

Figure S13. ^{1}H NMR spectrum of [{Dy(Cp*)$_2$(μ-Me$_4$Al)}$_2$] in C_6D_5Cl, zoomed in the region +200 to –200 ppm.

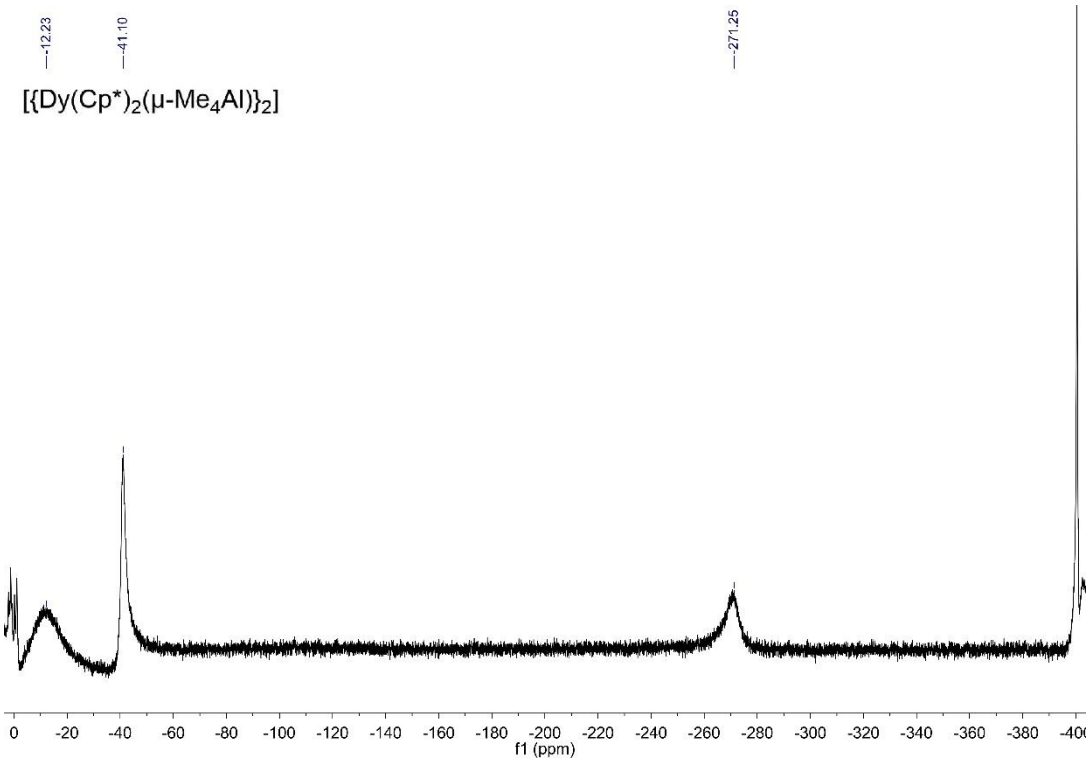

Figure S14. ^{1}H NMR spectrum of [{Dy(Cp*)$_2$(μ-Me$_4$Al)}$_2$] in C_6D_5Cl, zoomed in the region 0 to –400 ppm.

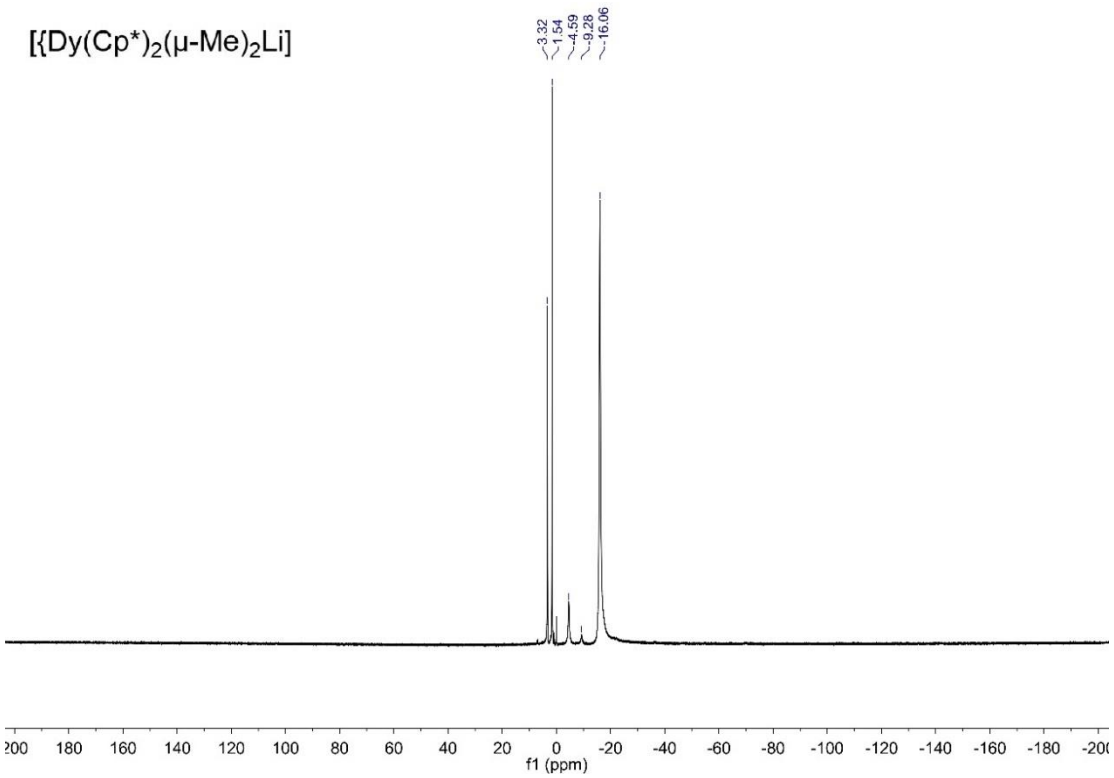

Figure S15. ^{1}H NMR spectrum of [Dy(Cp*)$_2$(μ-Me)$_2$Li] in C_6D_5Cl, zoomed in the region +200 to –200 ppm; no other signals were observed between +400 to –400 ppm.

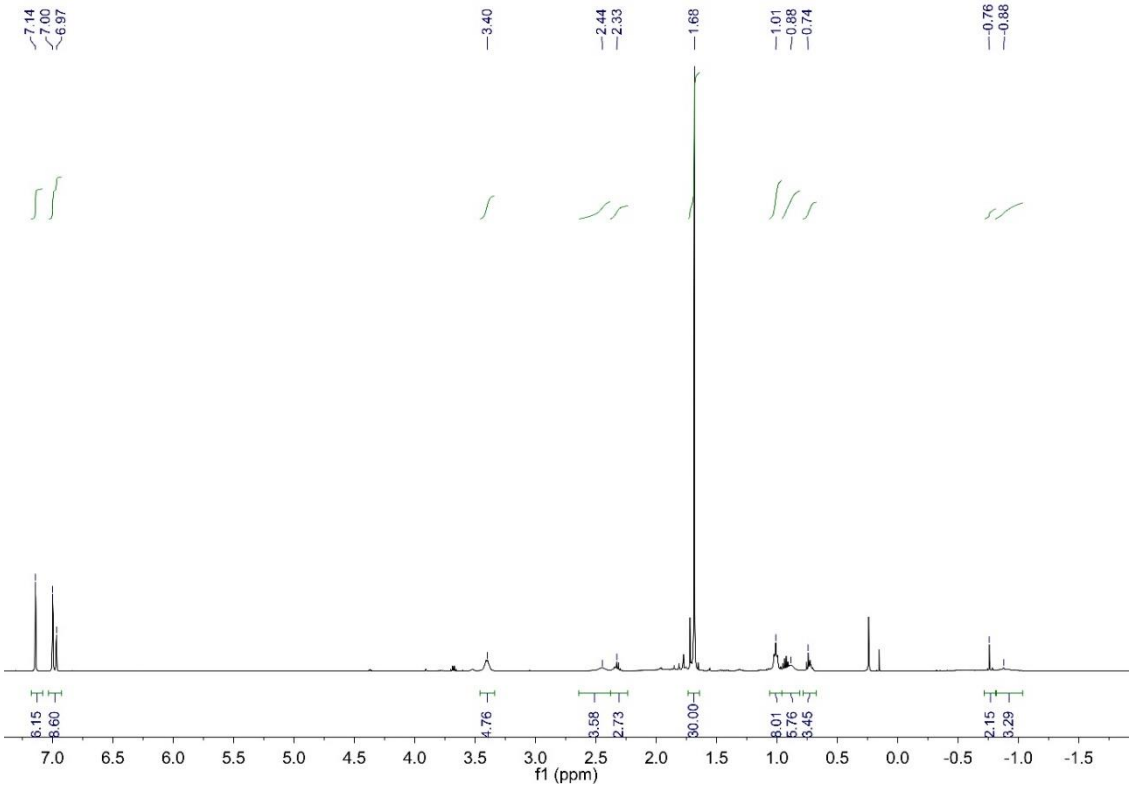

Figure S16. ^{1}H NMR spectrum of a sample of **1-Y** treated with diethyl ether, with volatiles removed *in vacuo* and the resultant tacky solid dissolved in C_6D_5Cl.

5. ATR-IR spectroscopy

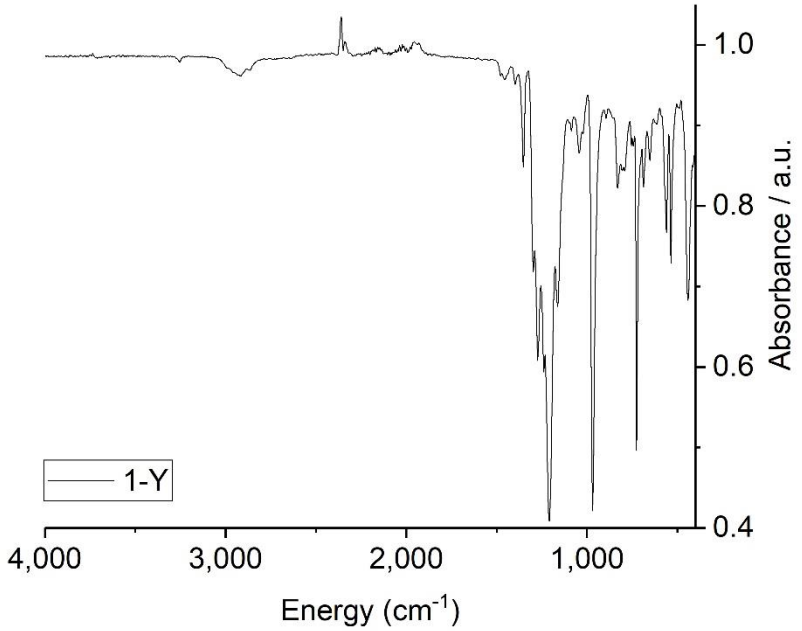

Figure S17. ATR-IR spectrum of **1-Y** recorded as a microcrystalline powder.

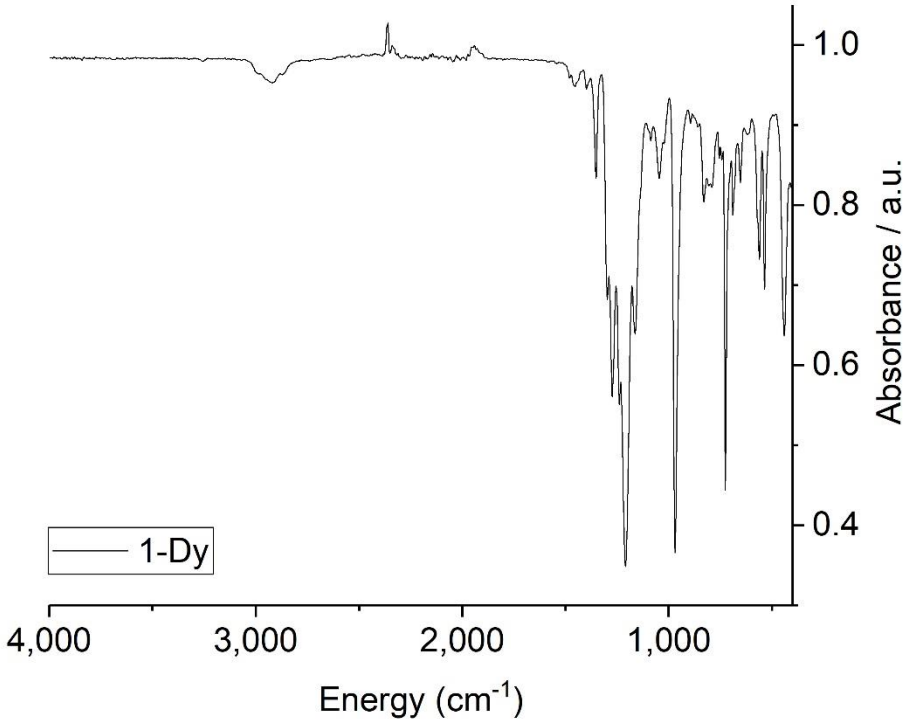

Figure S18. ATR-IR spectrum of **1-Dy** recorded as a microcrystalline powder.

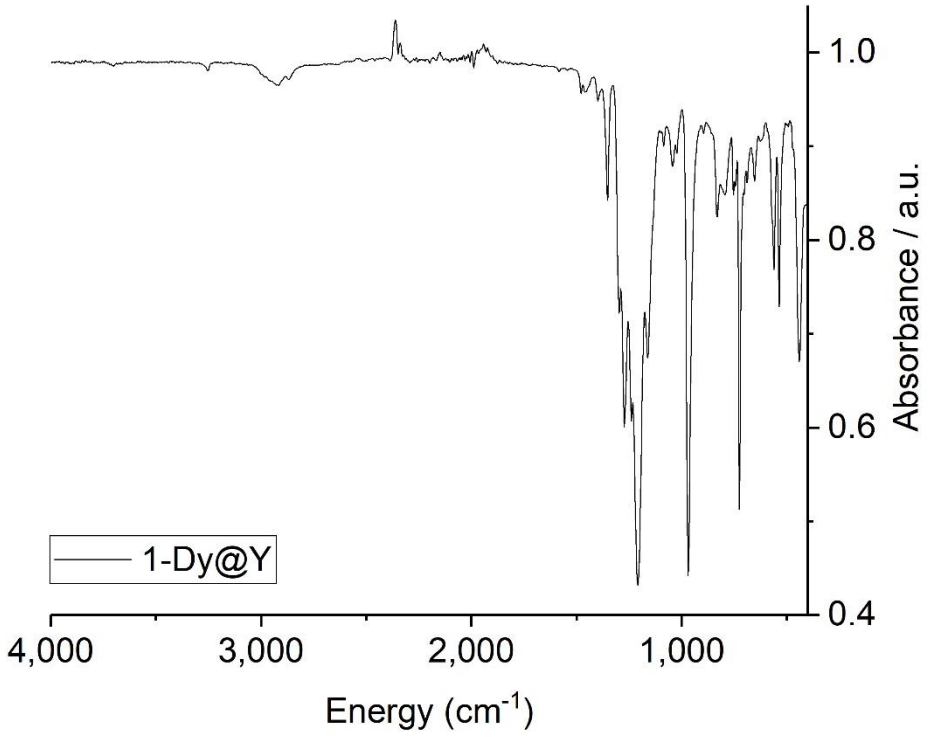

Figure S19. ATR-IR spectrum of **1-Dy@Y** recorded as a microcrystalline powder.

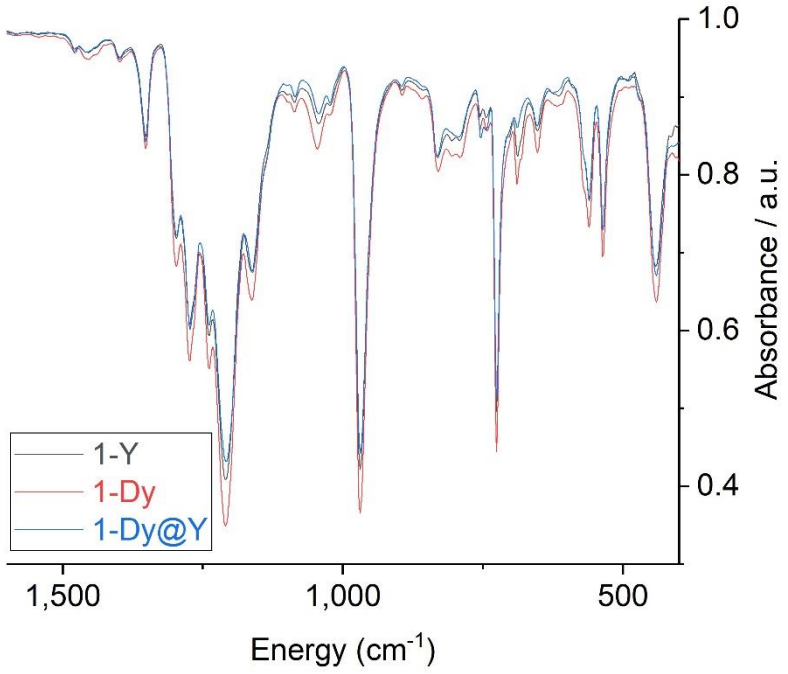

Figure S20. ATR-IR spectra of **1-Y**, **1-Dy** and **1-Dy@Y** in the region 1600–400 cm^{-1} intended to show the similarities between all spectra.

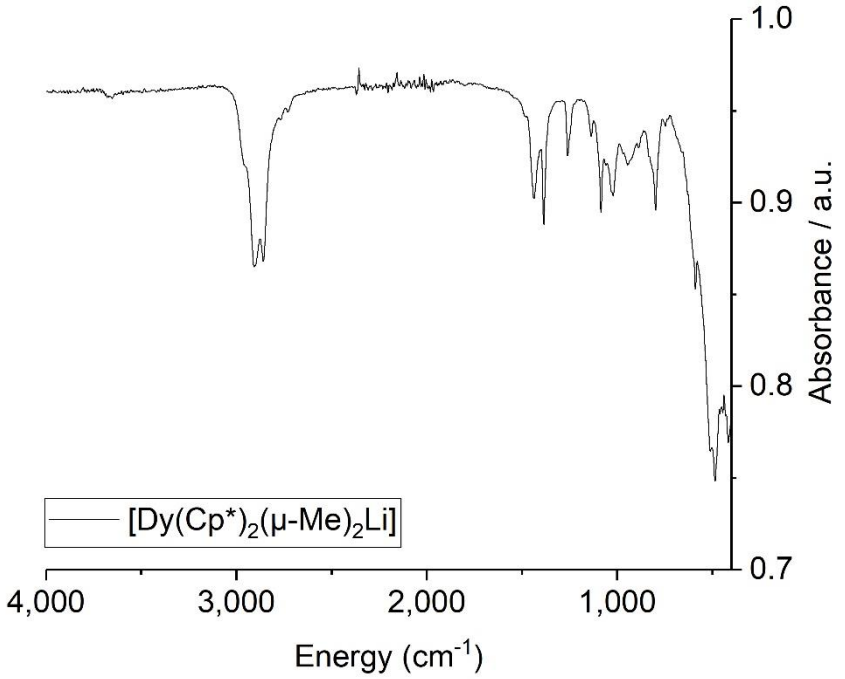

Figure S21. ATR-IR spectrum of $[Dy(Cp^*)_2(\mu\text{-}Me)_2Li]$ recorded as a microcrystalline powder.

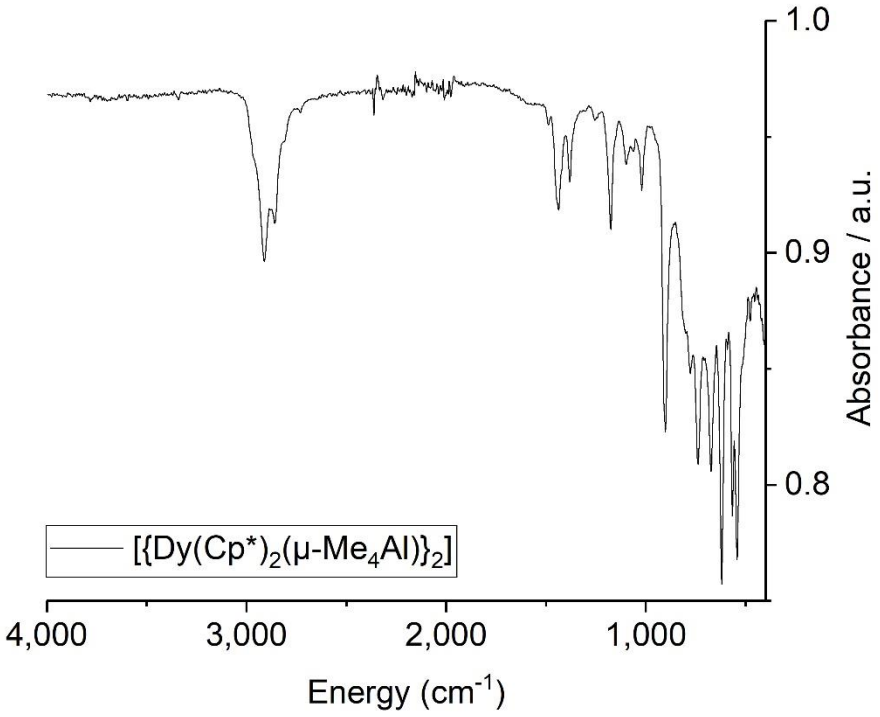

Figure S22. ATR-IR spectrum of $[\{Dy(Cp^*)_2(\mu\text{-}Me_4Al)\}_2]$ recorded as a microcrystalline powder.

6. Magnetic measurements

Magnetic measurements were made using a Quantum Design MPMS-XL7 superconducting quantum interference device (SQUID) magnetometer. All samples were prepared in the same manner. All samples for analysis by SQUID were exposed to dynamic vacuum (10^{-2} Torr) for 1 hour. As the crystalline appearance of the samples did not change we assume that the formulations are still **1-Ln.3C$_6$H$_5$Cl**, with no lattice solvent removed. Given that elemental analysis of **1-Ln.3C$_6$H$_5$Cl** gave reproducibly low carbon values that we have attributed to carbide formation, this uncertainty does not give us confidence that we can accurately determine the remaining lattice solvation by this method. Unfortunately, as C_6D_5Cl is the only NMR solvent that we were able to employ, we are also unable to determine solvation by integration of the ^{1}H NMR spectrum of **1-Y**. However, given the relatively large molecular weights of **1-Ln** (> 3,000 g/mol), the errors introduced into the calculations of magnetization and magnetic susceptibility for **1-Ln** vs. **1-Ln.3C$_6$H$_5$Cl** are relatively small, especially compared to those already present in such measurements. In order to best match the magnetization and susceptibility values to the calculated CASSCF results, we have employed a molecular weight that contains three chlorobenzene solvent molecules. This is justified by the fact that the CASSCF traces have the correct profiles, and the molecular weight simply acts as a scaling factor. All samples were crushed with a mortar and pestle under an inert atmosphere, and then loaded into a borosilicate glass NMR tube along with *ca.* powdered eicosane, which was then evacuated and flame-sealed to a length of *ca.* 5 cm. The eicosane was melted by heating the tube gently with a low-power heat gun in order to immobilize the crystallites. The NMR tube was then mounted in the centre of a drinking straw using friction by wrapping it with Kapton tape, and the straw was then fixed to the end of the sample rod. For **[{Dy(Cp*)$_2$(μ-Me$_4$Al)}$_2$]**, 29.8 mg of sample were prepared with 20.0 mg of eicosane; For **1-Dy**, 32.3 mg of desolvated sample were mixed with 15.8 mg of eicosane. The effect of intramolecular magnetic interactions was addressed by measuring two differently prepared doped samples (see section 1 for full details): one containing 34.8 mg of a 5:95 ratio of Dy:Y (**1-Dy@Y**) was prepared with 16.8 mg of powdered eicosane – the other contained 36.9 mg of a 5:95 ratio of Dy:Y (**1-Dy@Y_2**) and 16.9 mg of eicosane. The measurements were corrected for the diamagnetism of the straw, borosilicate tube and eicosane using calibrated blanks, and the intrinsic diamagnetism of the sample using Pascals constants.[9]

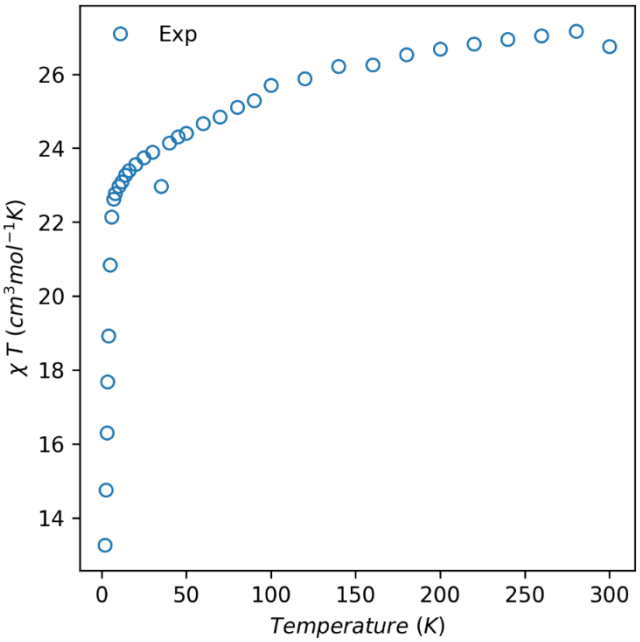

Figure S23. Temperature dependence of the molar magnetic susceptibility $\chi_M T$ products of **[{Dy(Cp*)$_2$(μ-Me$_4$Al)}$_2$]** measured under a 0.1 T DC field.

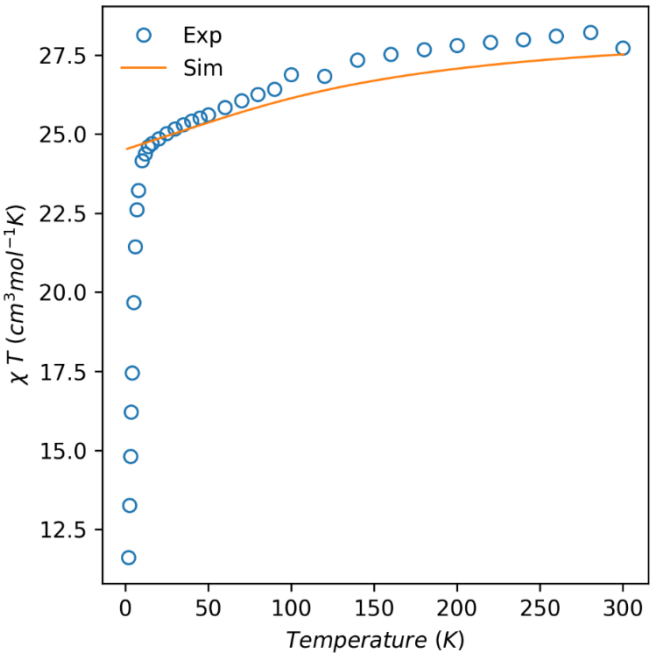

Figure S24. Temperature dependence of the molar magnetic susceptibility $\chi_M T$ products of **1-Dy** measured under a 0.1 T DC field. Simulated data obtained from CASSCF calculation and multiplied by two, as the calculation only considered one Dy(III) centre.

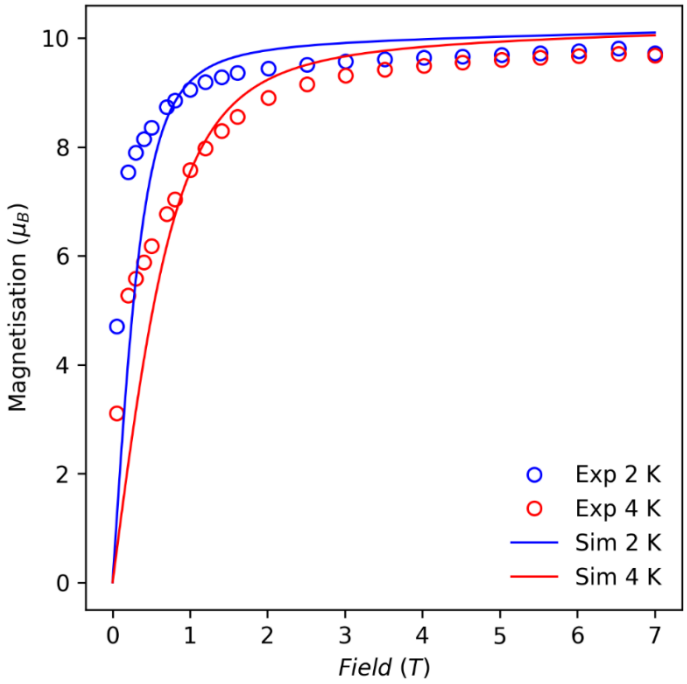

Figure S25. Magnetisation curves of **1-Dy**. Simulated data obtained from CASSCF calculation and multiplied by two, as the calculation only considered one Dy(III) centre.

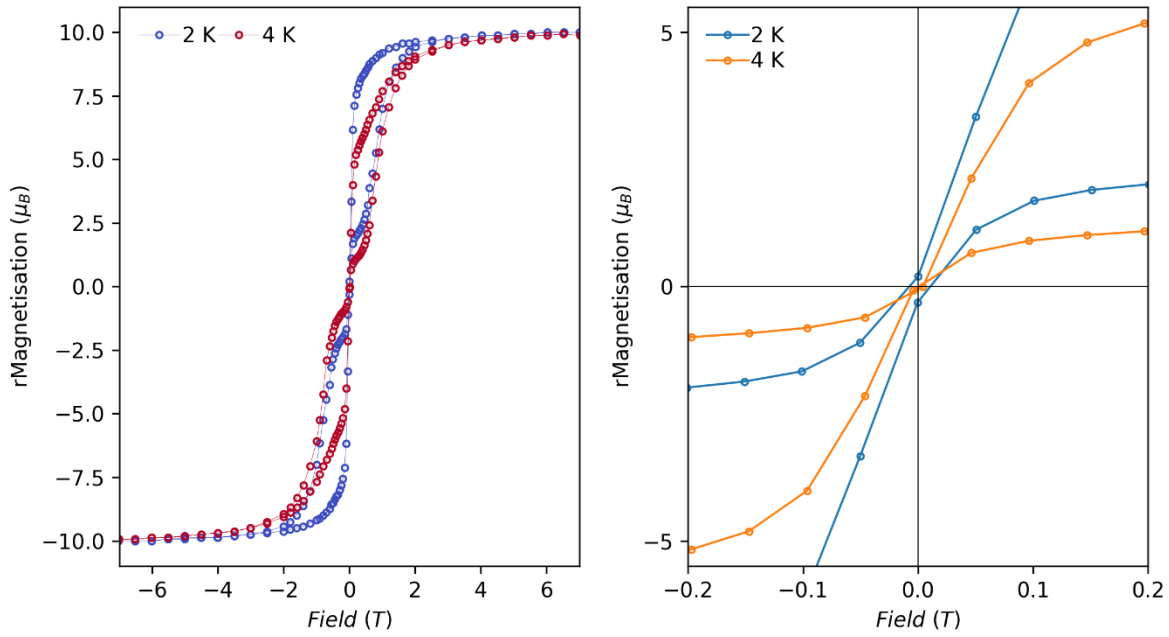

Figure S26. Temperature dependence of hysteresis loops of **[{Dy(Cp*)$_2$(μ-Me$_4$Al)}$_2$]**, showing closed loops at 4 K.

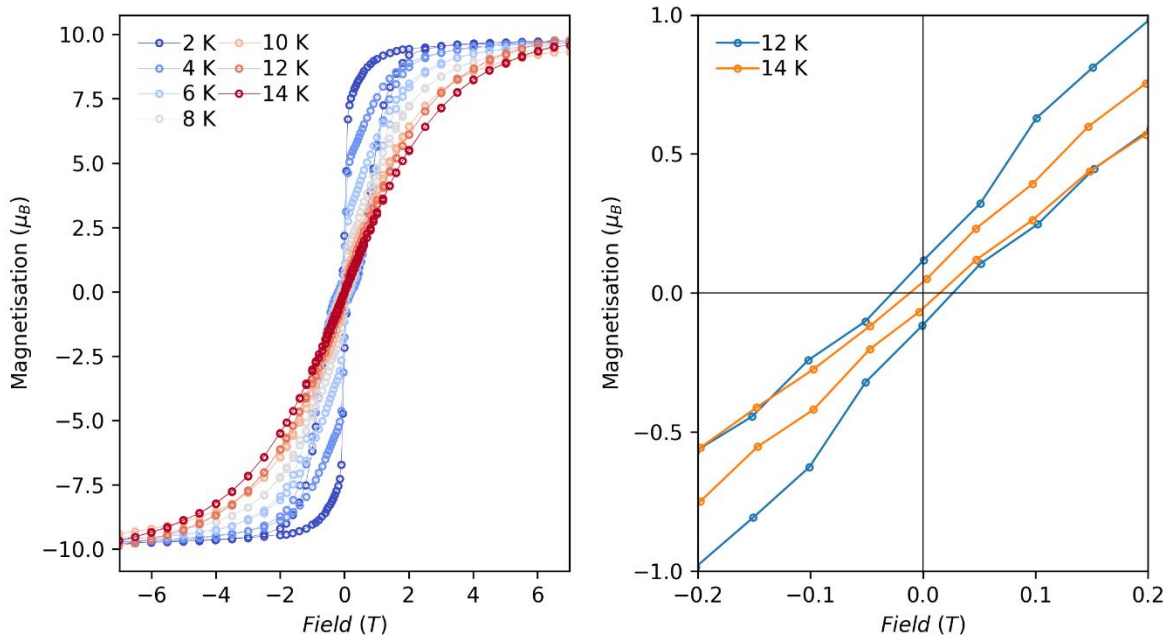

Figure S27. Temperature dependence of hysteresis loops of **1-Dy**, showing an opening up to 12 K.

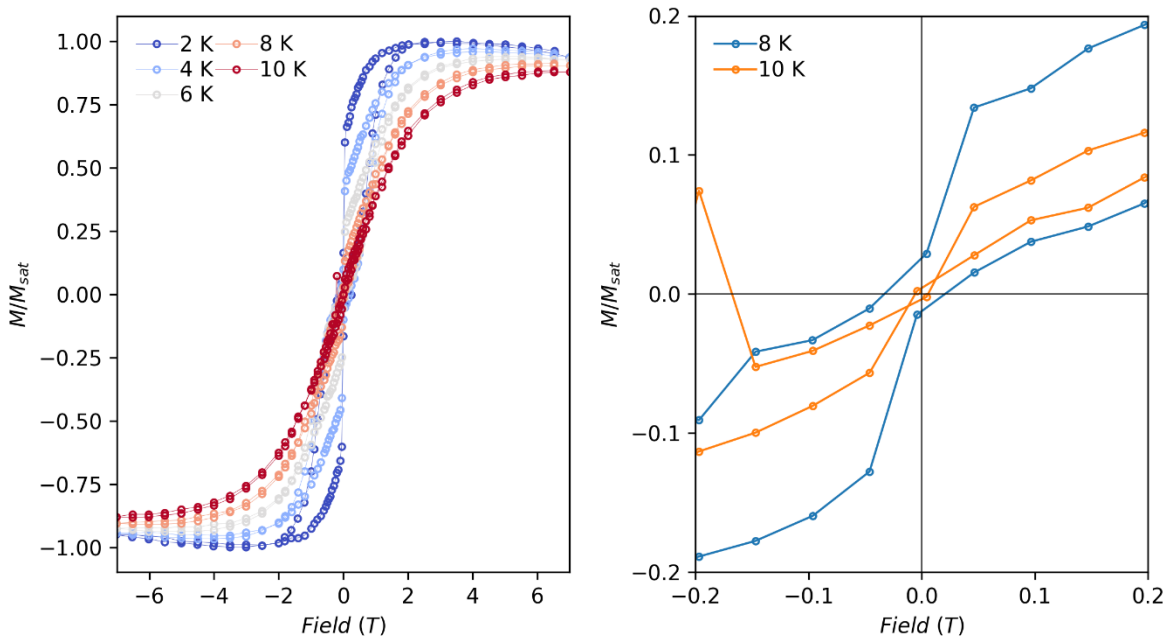

Figure S28. Temperature dependence of hysteresis loops of **1-Dy@Y**, showing an open loop at 8 K, but a closed loop and noisy data at 10 K.

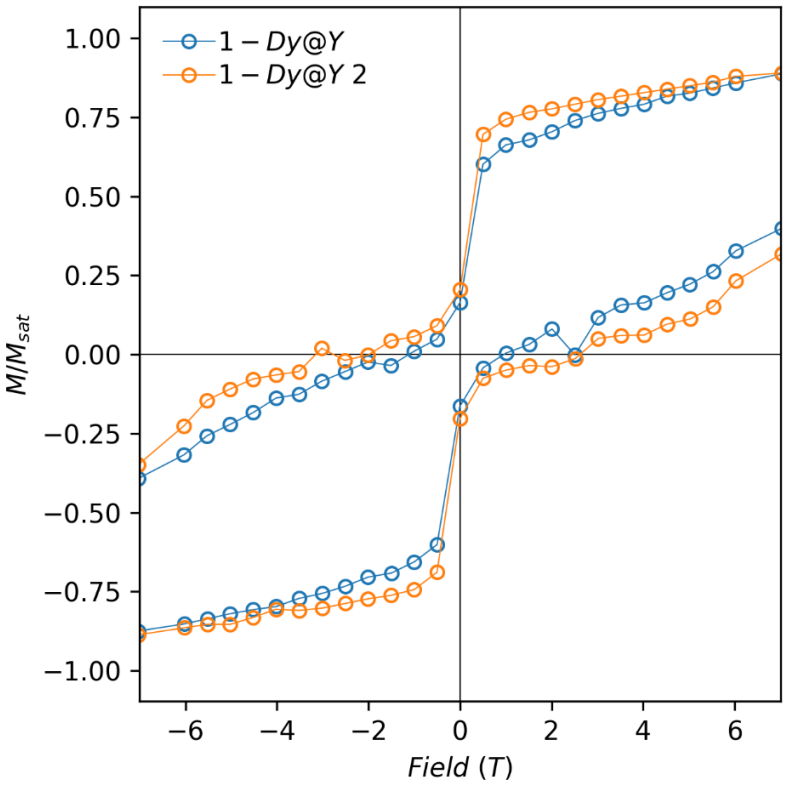

Figure S29. Comparison of 2 K hysteresis loops of **1-Dy@Y** and **1-Dy@Y_2**.

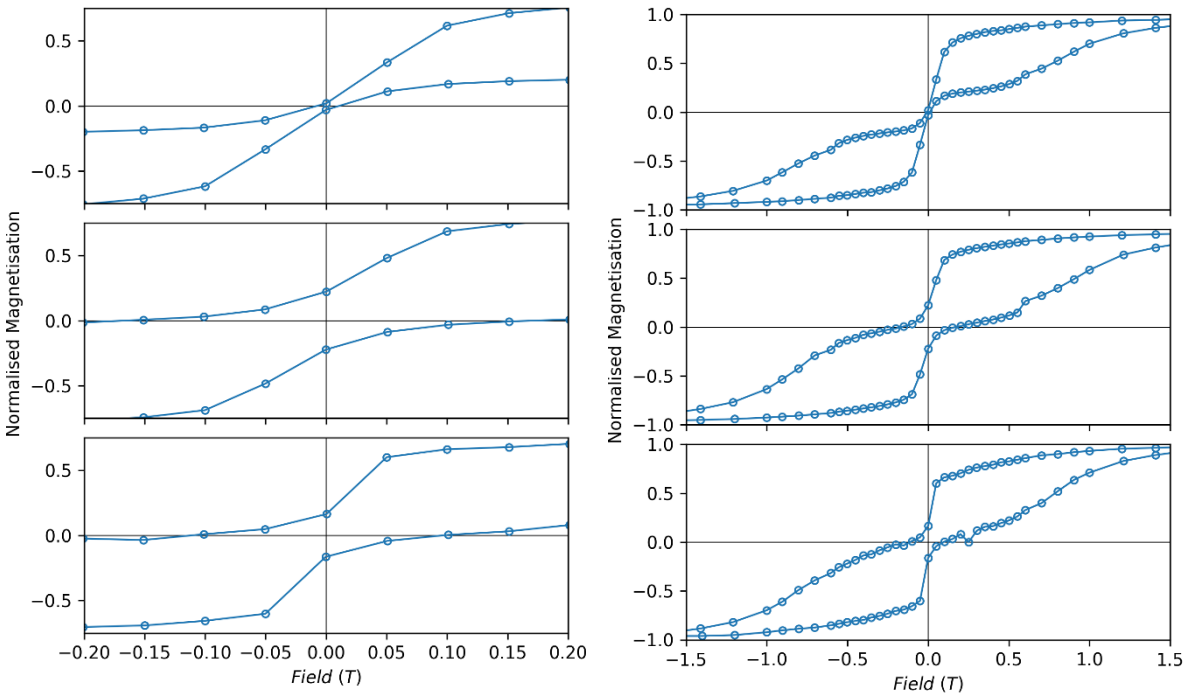

Figure S30. Comparison of 2 K hysteresis loops for **[{Dy(Cp*)$_2$(μ-Me$_4$Al)}$_2$]** (top), **1-Dy** (middle) and **1-Dy@Y** (bottom). Left and right columns show the field between ±0.2 and ±1.5 T, respectively.

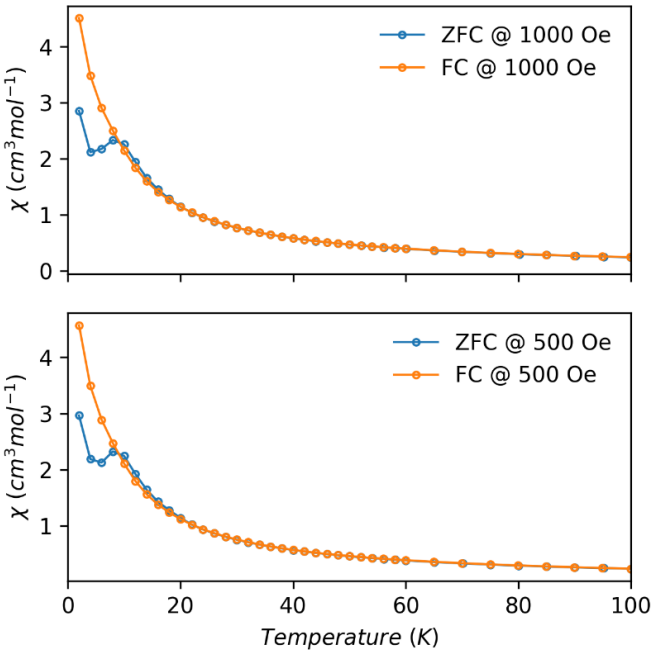

Figure S31. Zero-field cooled (ZFC), field cooled (FC) measurements of **1-Dy** under a 0.1 T (top) and 0.05 T (bottom) external field, showing a maximum at 8 K.

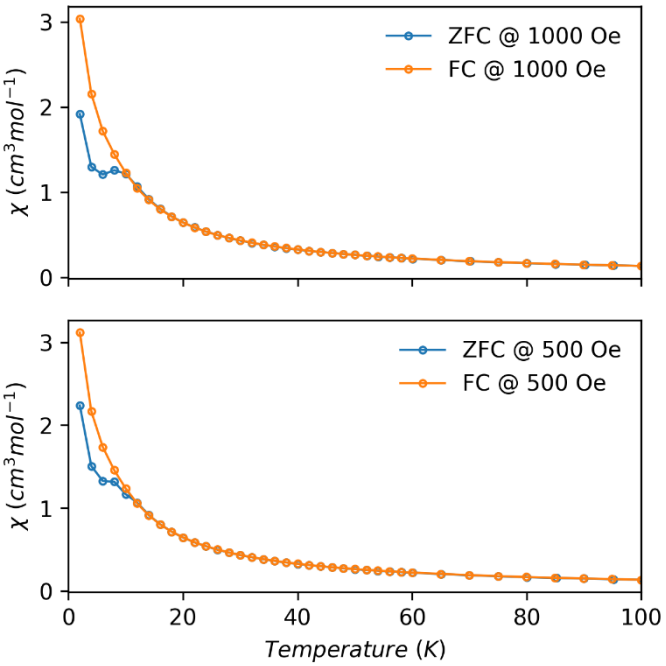

Figure S32. Zero-field cooled (ZFC), field cooled (FC) measurements of **1-Dy@Y** under a 0.1 T (top) and 0.05 T (bottom) external field, showing a maximum at 8 K. The data have been scaled and the diamagnetic corrections determined in order to best match the susceptibility data of **1-Dy** for each data set.

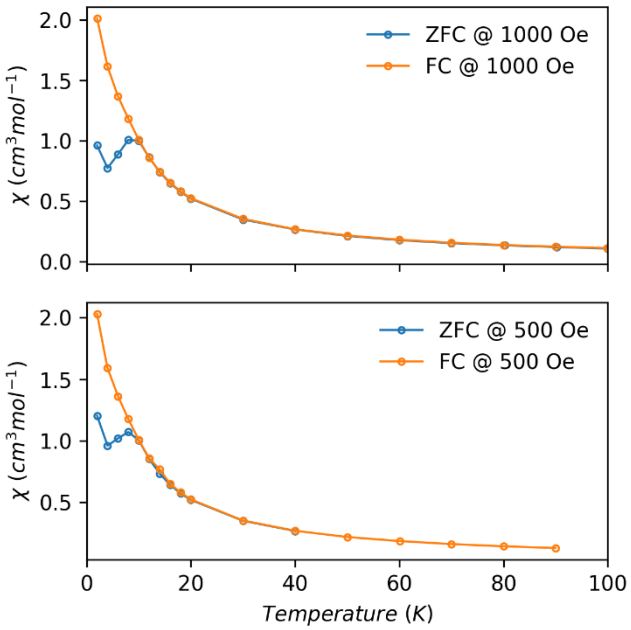

Figure S33. Zero-field cooled (ZFC), field cooled (FC) measurements of **1-Dy@Y_2** under a 0.1 T (top) and 0.05 T (bottom) external field, showing a maximum at 8 K. The data have been scaled and the diamagnetic corrections determined in order to best match the susceptibility data of **1-Dy** for each data set.

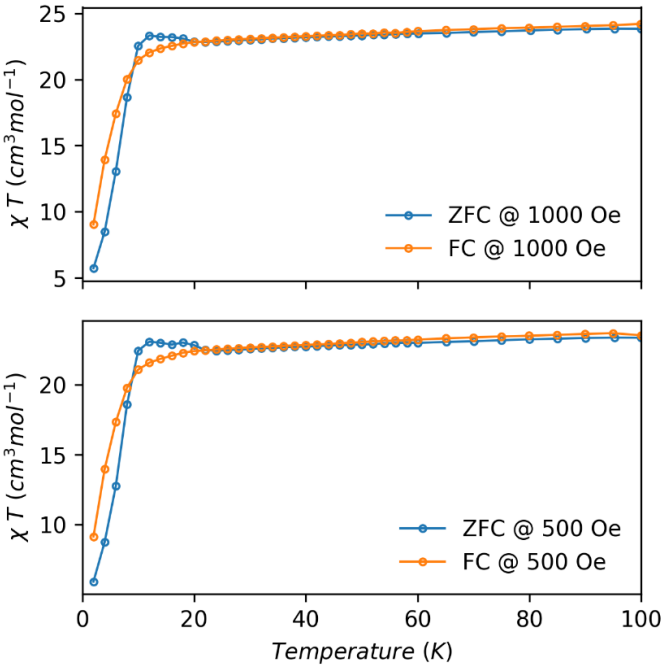

Figure S34. Zero-field cooled (ZFC), field cooled (FC) measurements of **1-Dy** under a 0.1 T (top) and 0.05 T (bottom) external field. The curves overlap at 22 K.

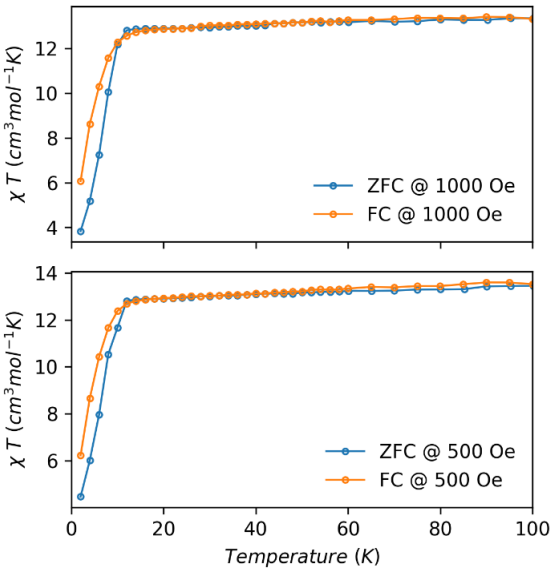

Figure S35. Zero-field cooled (ZFC), field cooled (FC) measurements of **1-Dy@Y** under a 0.1 T (top) and 0.05 T (bottom) external field. The curves overlap at 13 K. The data have been scaled and the diamagnetic corrections determined in order to best match the susceptibility data of **1-Dy** for each data set.

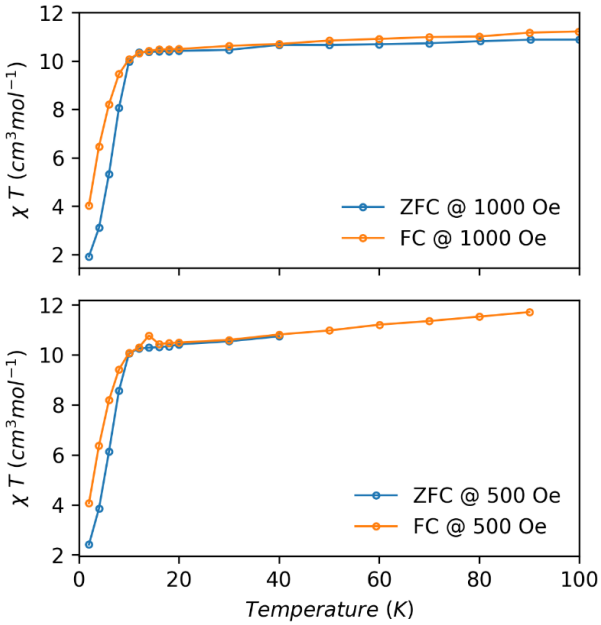

Figure S36. Zero-field cooled (ZFC), field cooled (FC) measurements of **1-Dy@Y_2** under a 0.1 T (top) and 0.05 T (bottom) external field. The curves overlap at 13 K. The data have been scaled and the diamagnetic corrections determined in order to best match the susceptibility data of **1-Dy** for each data set.

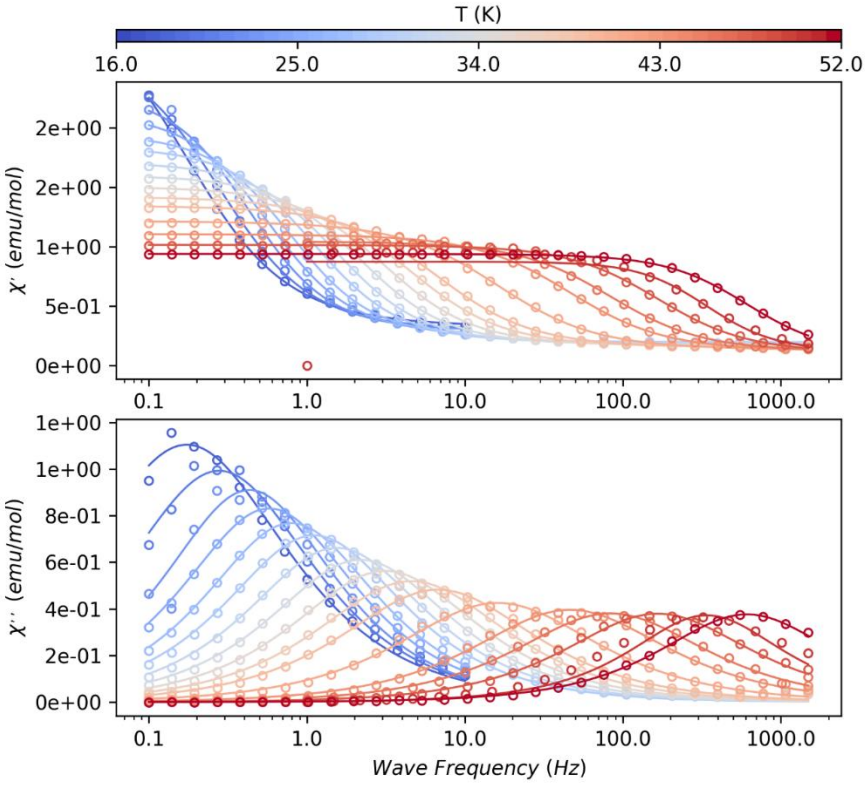

Figure S37. In-phase (top) and out-of-phase (bottom) ac susceptibilities of **[{Dy(Cp*)$_2$(μ-Me$_4$Al)}$_2$]** in a zero field. Solid lines are fits to the generalized Debye model, giving $0.001 \leq \alpha \leq 0.16$.

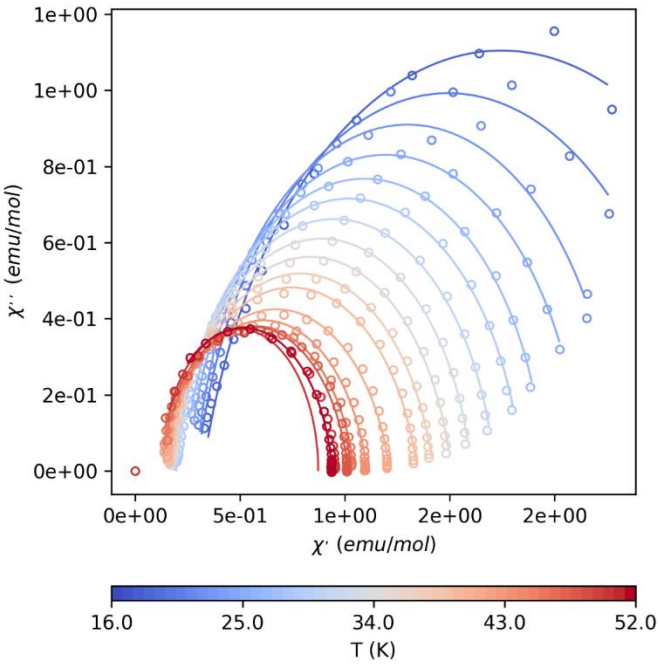

Figure S38. Cole-Cole plot for **[{Dy(Cp*)$_2$(μ-Me$_4$Al)}$_2$]**. Solid lines are fits to the generalized Debye model, giving $0.001 \leq \alpha \leq 0.16$.

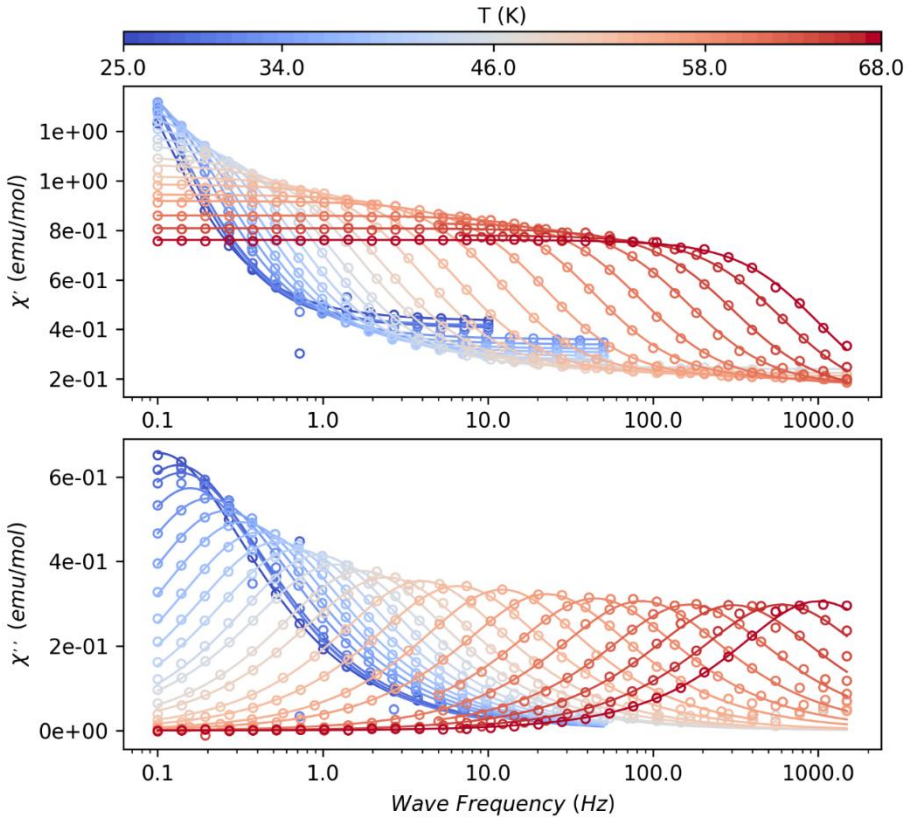

Figure S39. In-phase (top) and out-of-phase (bottom) ac susceptibilities of **1-Dy** in a zero field. Solid lines are fits to the generalized Debye model, giving $0.002 \leq \alpha \leq 0.1$.

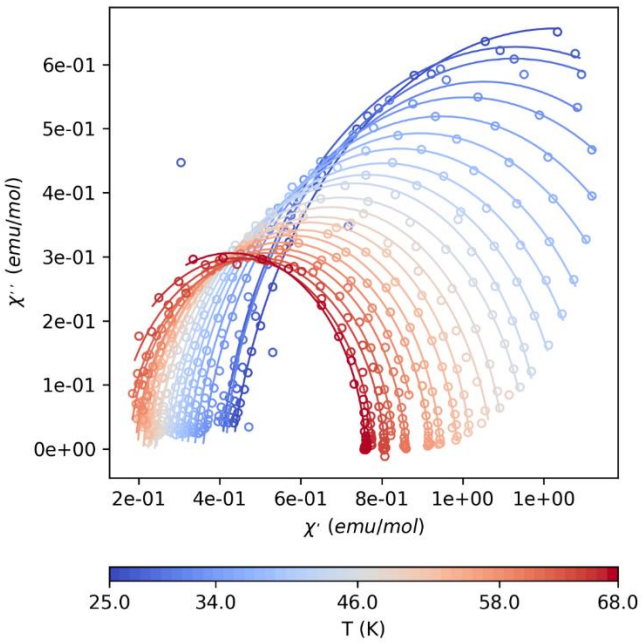

Figure S40. Cole-Cole plot for **1-Dy**. Solid lines are fits to the generalized Debye model, giving $0.002 \leq \alpha \leq 0.1$.

Table S3. Best fit parameters to the generalized Debye model for **[{Dy(Cp*)$_2$(μ-Me$_4$Al)}$_2$]**.

T	τ	$\tau_{LN}^{err\_upper}$	$\tau_{LN}^{err\_lower}$	τ_{Debye}^{err}	χ_S	χ_S^{err}	χ_T	χ_T^{err}	α	α^{err}
(K)		(s)				(emu/mol)				
16.00	9.16E-01	2.18E+00	3.85E-01	3.12E-02	3.22E-01	1.25E-02	3.17E+00	5.74E-02	0.160	1.25E-02
18.00	5.72E-01	1.17E+00	2.80E-01	1.19E-02	2.94E-01	1.10E-02	2.69E+00	3.08E-02	0.119	1.04E-02
20.00	3.68E-01	6.03E-01	2.24E-01	1.27E-02	2.92E-01	2.30E-02	2.31E+00	4.28E-02	0.064	2.16E-02
22.00	2.76E-01	4.79E-01	1.59E-01	2.16E-03	2.53E-01	5.53E-03	2.13E+00	8.27E-03	0.078	4.97E-03
24.00	2.00E-01	3.37E-01	1.19E-01	1.25E-03	2.34E-01	4.66E-03	1.95E+00	5.49E-03	0.071	4.08E-03
26.00	1.43E-01	2.60E-01	7.88E-02	1.37E-03	1.96E-01	3.21E-03	1.84E+00	7.39E-03	0.089	5.19E-03
28.00	1.03E-01	1.88E-01	5.62E-02	8.78E-04	1.85E-01	2.82E-03	1.71E+00	5.65E-03	0.091	4.63E-03
30.00	7.27E-02	1.38E-01	3.83E-02	5.79E-04	1.73E-01	2.57E-03	1.60E+00	4.54E-03	0.100	4.26E-03
32.00	5.07E-02	1.00E-01	2.56E-02	4.65E-04	1.64E-01	2.89E-03	1.51E+00	4.51E-03	0.111	4.82E-03
34.00	3.48E-02	7.26E-02	1.67E-02	2.91E-04	1.55E-01	2.58E-03	1.42E+00	3.56E-03	0.125	4.30E-03
36.00	2.35E-02	5.11E-02	1.09E-02	2.31E-04	1.49E-01	3.01E-03	1.34E+00	3.65E-03	0.135	4.97E-03
40.00	9.86E-03	2.28E-02	4.26E-03	1.15E-04	1.30E-01	3.65E-03	1.21E+00	3.33E-03	0.153	5.74E-03
44.00	3.44E-03	7.51E-03	1.57E-03	3.50E-05	1.20E-01	3.56E-03	1.10E+00	2.27E-03	0.137	5.13E-03

46.00	1.91E-03	4.00E-03	9.09E-04	2.85E-05	1.15E-01	5.55E-03	1.04E+00	3.90E-03	0.126	8.03E-03
48.00	9.58E-04	1.92E-03	4.77E-04	1.08E-05	1.05E-01	4.87E-03	1.01E+00	1.86E-03	0.115	5.74E-03
50.00	4.69E-04	5.03E-04	4.39E-04	1.18E-04	1.26E-01	1.23E-01	8.72E-01	4.51E-02	0.001	1.59E-01
52.00	2.61E-04	4.46E-04	1.53E-04	2.84E-06	9.15E-02	5.99E-03	9.38E-01	1.04E-03	0.074	4.96E-03

Table S4. Best fit parameters to the generalized Debye model for **1-Dy**.

T	τ	$\tau_{LN}^{err\_upper}$	$\tau_{LN}^{err\_lower}$	τ_{Debye}^{err}	χ_S	χ_S^{err}	χ_T	χ_T^{err}	α	α^{err}
(K)		(s)				(emu/mol)				
25.00	1.570E+00	3.26E+00	7.55E-01	3.17E-02	4.32E-01	2.37E-03	2.03E+00	2.04E-02	0.124	5.87E-03
26.00	1.203E+00	2.21E+00	6.54E-01	1.70E-01	4.05E-01	2.25E-02	1.86E+00	1.38E-01	0.092	5.23E-02
27.00	1.152E+00	2.25E+00	5.88E-01	1.34E-02	4.03E-01	1.87E-03	1.85E+00	1.09E-02	0.108	4.25E-03
28.00	1.010E+00	1.68E+00	6.08E-01	1.25E-01	4.15E-01	2.25E-02	1.69E+00	1.11E-01	0.068	5.37E-02
30.00	7.850E-01	1.52E+00	4.05E-01	1.03E-02	3.58E-01	2.15E-03	1.65E+00	1.08E-02	0.105	5.48E-03
32.00	6.221E-01	1.19E+00	3.26E-01	6.55E-03	3.38E-01	1.99E-03	1.56E+00	8.05E-03	0.102	4.87E-03
34.00	4.922E-01	9.26E-01	2.62E-01	4.12E-03	3.20E-01	1.79E-03	1.47E+00	5.89E-03	0.098	4.20E-03
36.00	3.845E-01	6.99E-01	2.12E-01	2.71E-03	3.06E-01	1.67E-03	1.38E+00	4.51E-03	0.089	3.81E-03
38.00	2.996E-01	5.50E-01	1.63E-01	2.13E-03	2.90E-01	1.80E-03	1.32E+00	4.10E-03	0.092	3.96E-03
40.00	2.299E-01	4.13E-01	1.28E-01	1.61E-03	2.76E-01	1.89E-03	1.26E+00	3.62E-03	0.086	4.04E-03
42.00	1.702E-01	2.88E-01	1.01E-01	1.96E-03	2.67E-01	3.35E-03	1.20E+00	5.33E-03	0.072	6.93E-03
44.00	1.327E-01	2.54E-01	6.93E-02	2.75E-03	2.39E-01	3.85E-03	1.16E+00	8.67E-03	0.103	1.10E-02
46.00	9.191E-02	1.62E-01	5.22E-02	9.00E-04	2.44E-01	2.18E-03	1.10E+00	3.55E-03	0.082	5.51E-03

48.00	6.568E-02	1.25E-01	3.46E-02	1.30E-03	2.23E-01	3.86E-03	1.07E+00	6.56E-03	0.100	1.06E-02
50.00	4.005E-02	6.79E-02	2.36E-02	2.62E-04	2.27E-01	1.57E-03	1.02E+00	1.86E-03	0.072	3.73E-03
52.00	2.426E-02	4.26E-02	1.38E-02	3.57E-04	2.11E-01	3.14E-03	9.88E-01	3.79E-03	0.081	8.10E-03
54.00	1.304E-02	2.10E-02	8.08E-03	7.40E-05	2.11E-01	1.57E-03	9.45E-01	1.25E-03	0.061	3.30E-03
56.00	7.031E-03	1.19E-02	4.16E-03	8.83E-05	1.97E-01	3.05E-03	9.19E-01	2.53E-03	0.072	7.02E-03
58.00	3.566E-03	5.99E-03	2.12E-03	6.59E-05	1.91E-01	4.43E-03	8.89E-01	6.50E-03	0.070	1.14E-02
60.00	1.872E-03	3.14E-03	1.11E-03	2.78E-05	1.76E-01	4.39E-03	8.61E-01	2.33E-03	0.070	8.35E-03
62.00	9.615E-04	1.61E-03	5.74E-04	1.50E-05	1.66E-01	5.21E-03	8.31E-01	3.56E-03	0.070	9.58E-03
64.00	5.175E-04	8.85E-04	3.03E-04	8.20E-06	1.42E-01	6.09E-03	8.09E-01	1.75E-03	0.074	8.39E-03
66.00	2.649E-04	4.53E-04	1.55E-04	4.80E-06	1.11E-01	8.09E-03	7.81E-01	2.25E-03	0.074	9.13E-03
68.00	1.586E-04	2.51E-04	1.00E-04	3.18E-06	9.26E-02	9.42E-03	7.61E-01	1.03E-03	0.057	7.72E-03

Table S5. Best fit parameters to the magnetisation decay curves for **1-Dy** using a stretched exponential model function $M(t) = M_2 + (M_1 - M_2)exp^{-((t/\tau)^{\beta})}$. M_2, τ and α are the fitting parameters.

T	τ	β	M_2	M(t) vs t plots
10.00	169.383	0.833	2.01E-04	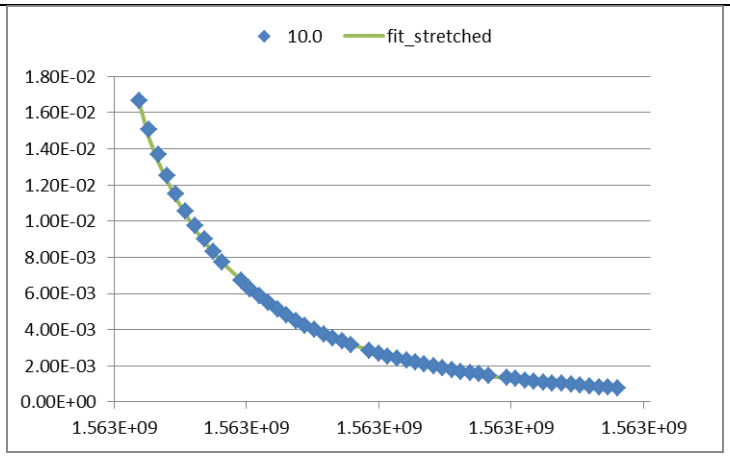
9.00	225.148	0.866	9.55E-04	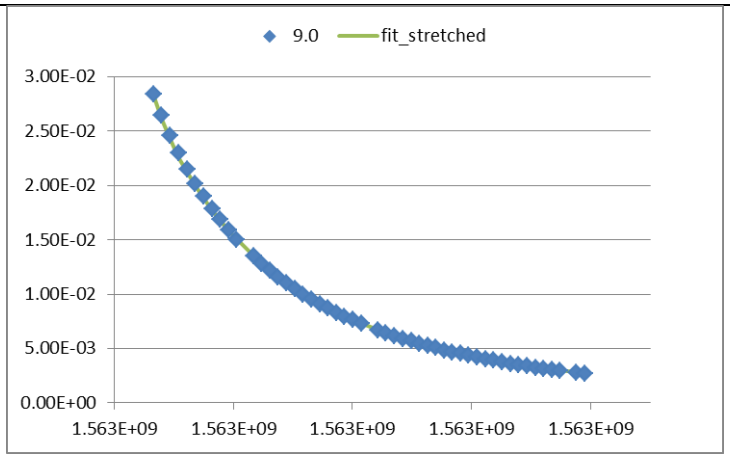
8.00	340.018	0.813	1.03E-03	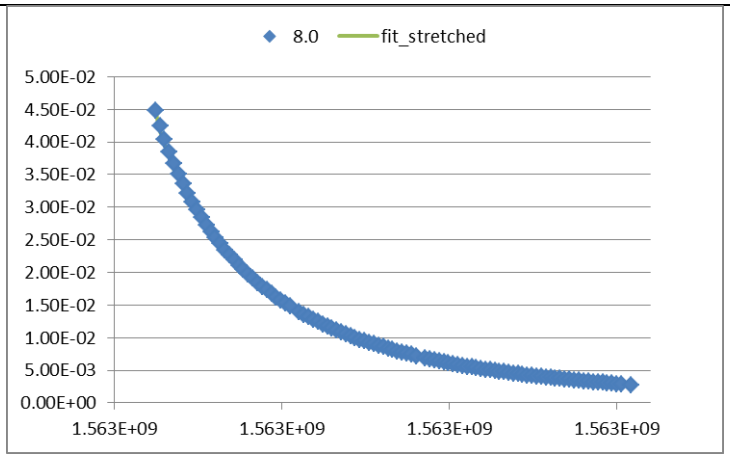

7.00	552.380	0.792	1.59E-03	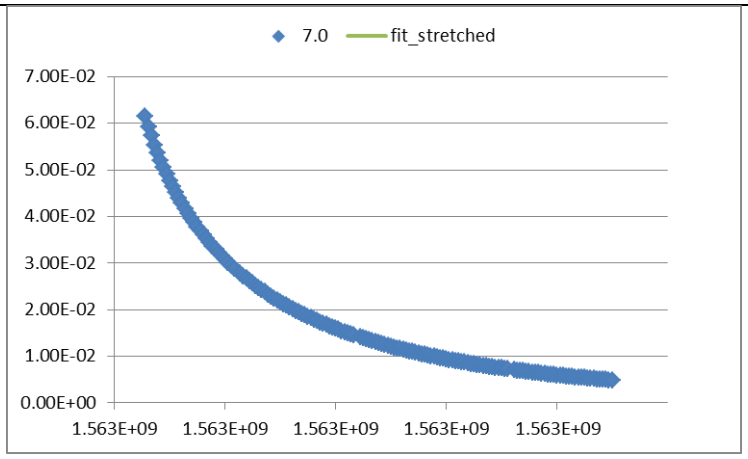
6.20	848.564	0.778	2.84E-03	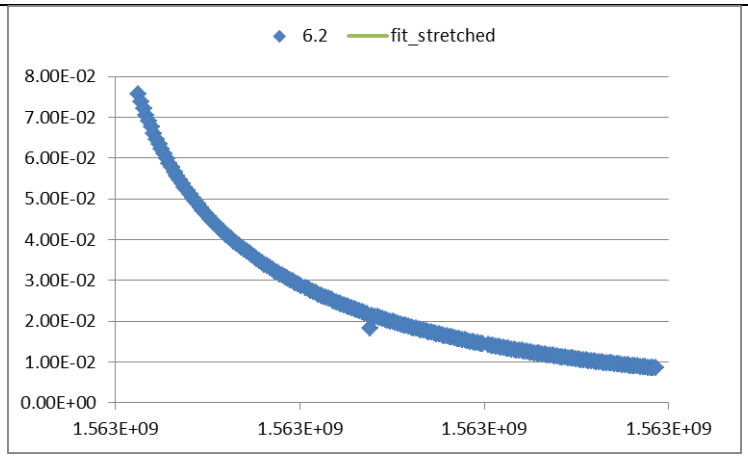
5.40	1514.542	0.731	2.59E-03	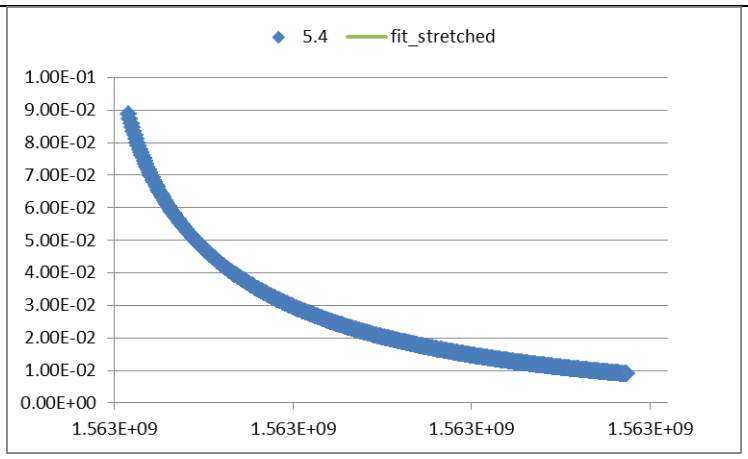

4.80	2480.993	0.701	2.90E-03	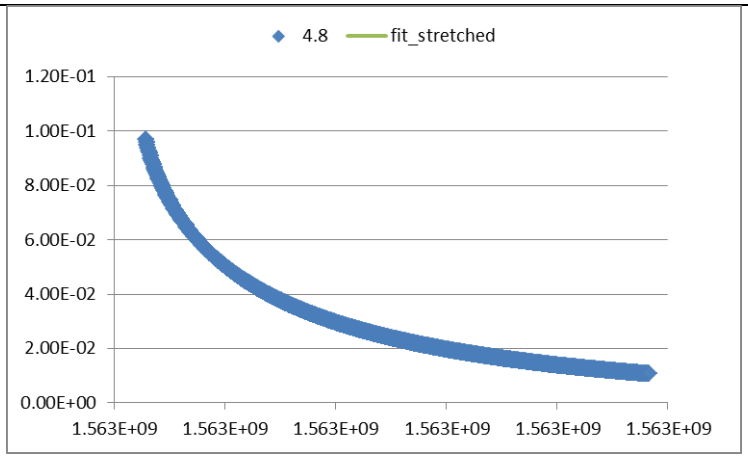
4.20	4461.396	0.663	2.89E-03	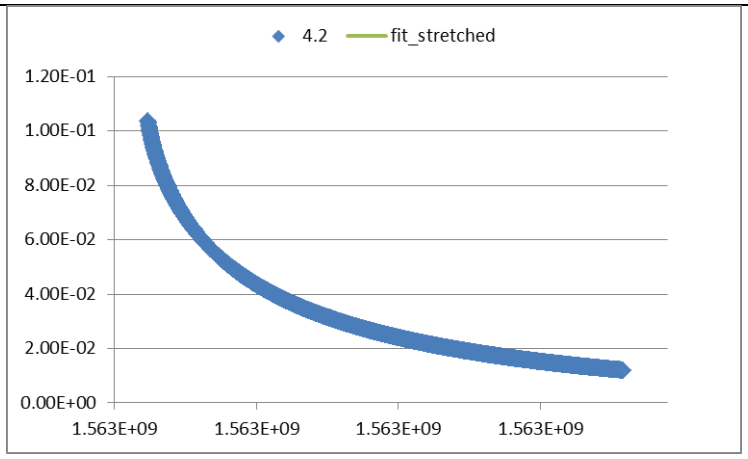
3.70	7952.794	0.625	2.65E-03	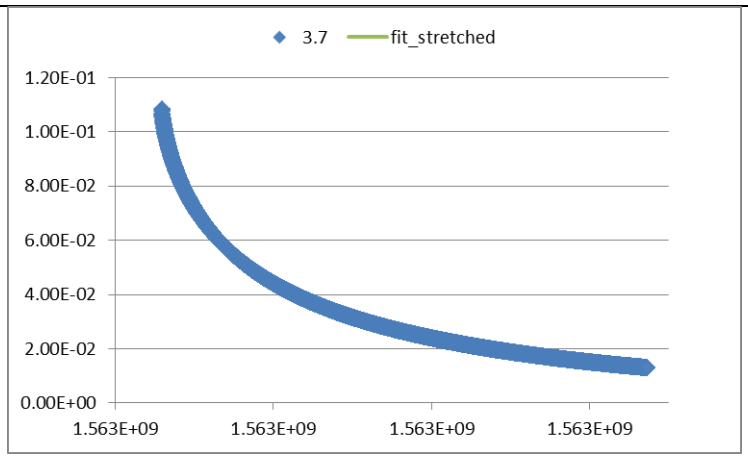

3.25	14269.790	0.587	2.59E-03	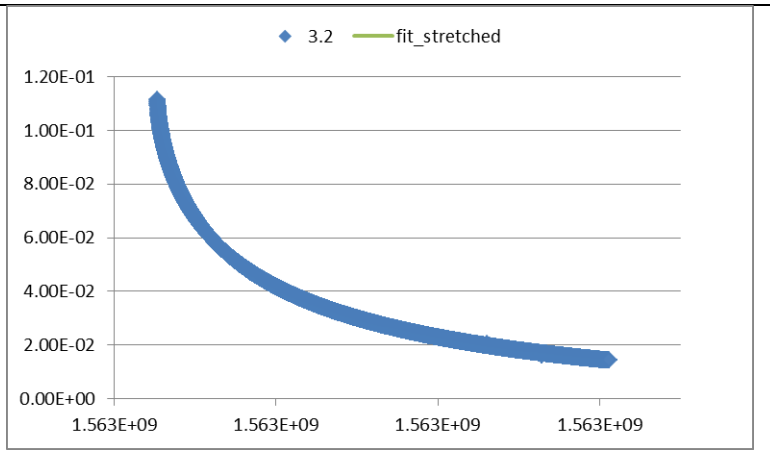
2.90	23288.330	0.555	2.51E-03	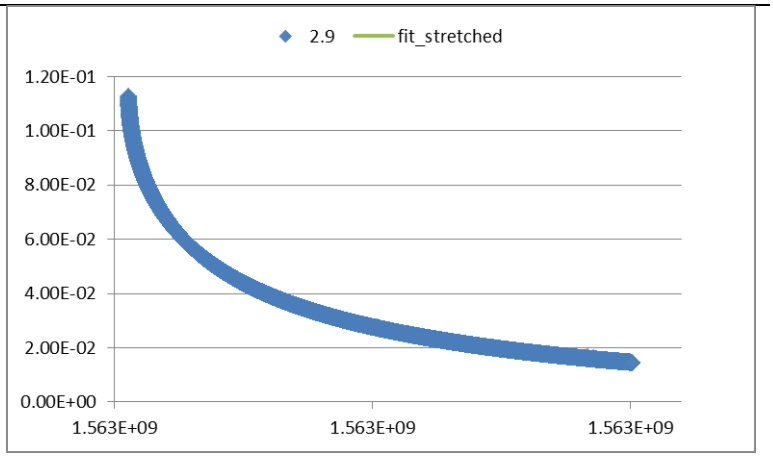
2.60	27906.488	0.563	1.09E-02	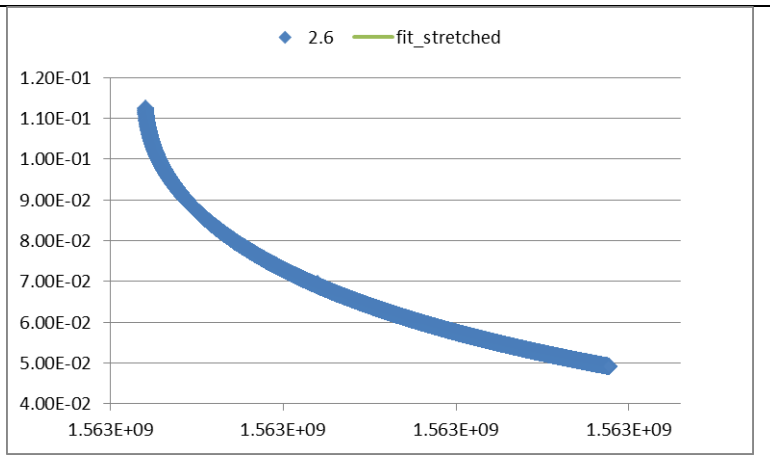

Table S6. Best fit parameters to the magnetisation decay curves for **1-Dy@Y** using a stretched exponential model function $M(t) = M_2 + (M_1 - M_2)exp^{-((t/\tau)^{\beta})}$. M_2, τ and α are the fitting parameters.

T	τ	β	M_2	M(t) vs t plots
7.00	200.000	0.666	0.00E+00	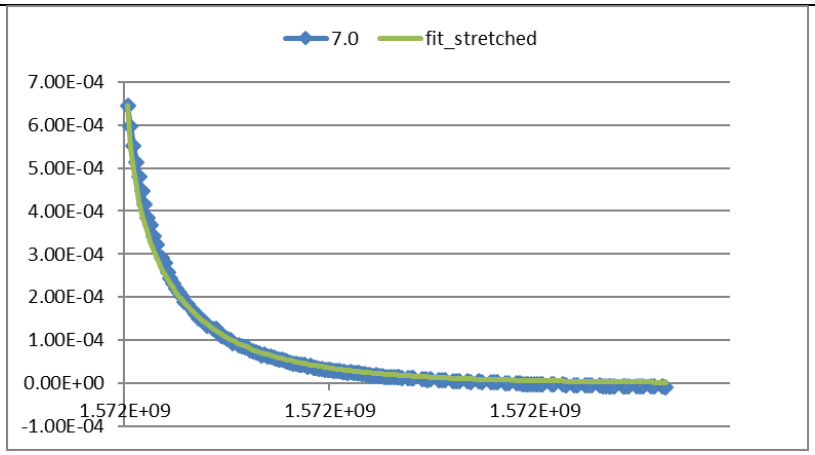
6.20	318.346	0.657	0.00E+00	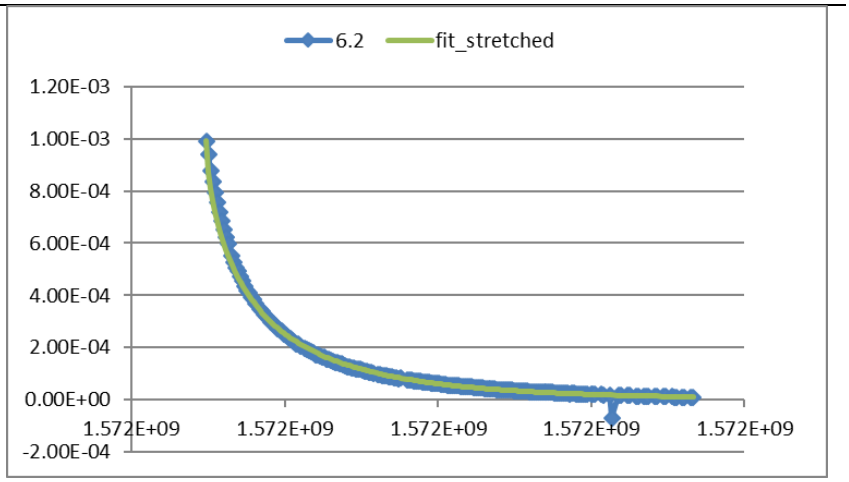
5.40	486.245	0.585	6.69E-07	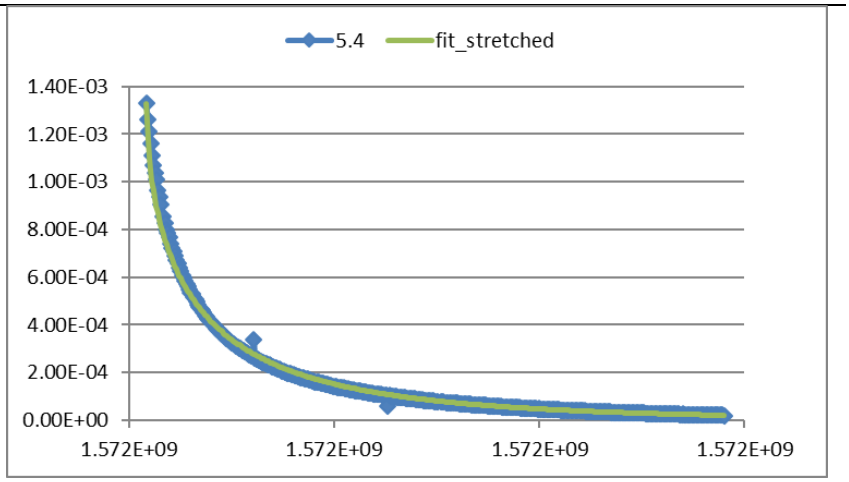

4.20	932.150	0.465	1.66E-06	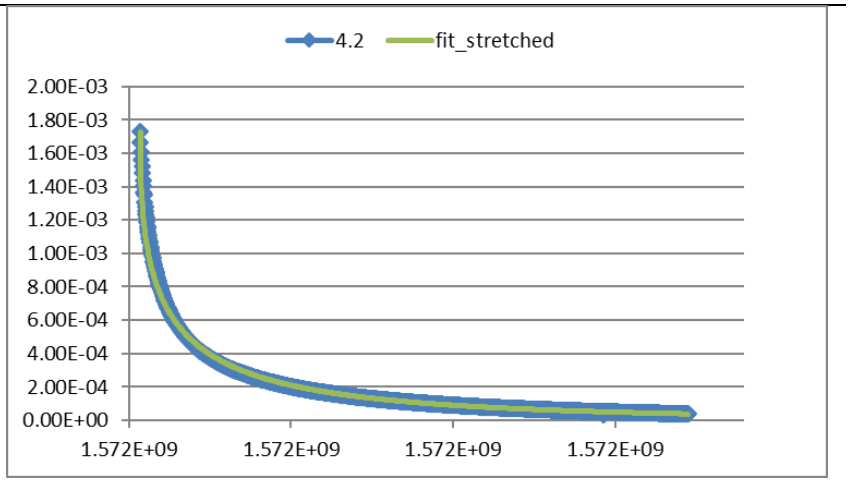
3.70	1425.555	0.436	1.13E-05	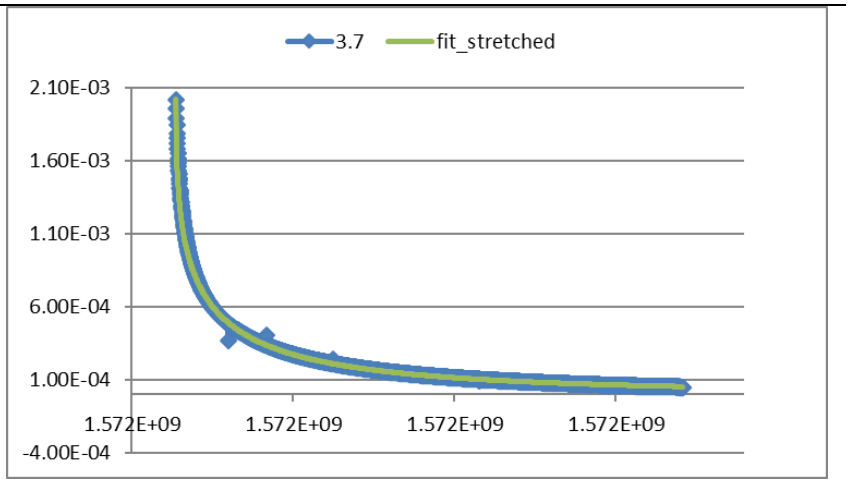
3.25	2102.039	0.382	1.15E-05	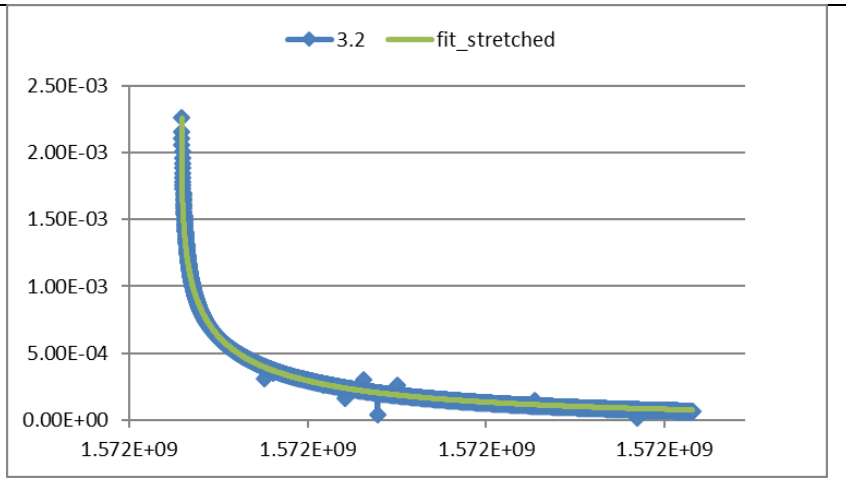

2.60	1758.841	0.343	2.53E-04

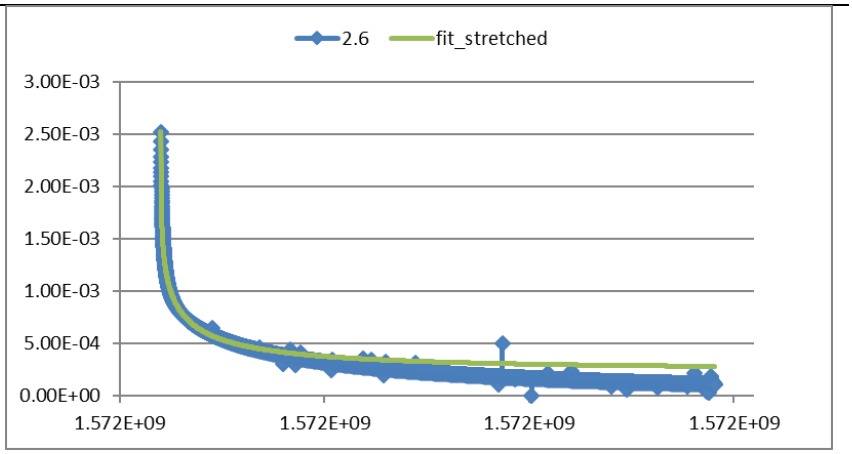

Table S7. Best fit parameters to the magnetisation decay curves for **1-Dy@Y_2** using a stretched exponential model function $M(t) = M_2 + (M_1 - M_2)exp^{-((t/\tau)^{\beta})}$. M_2, τ and α are the fitting parameters.

T	τ	β	M_2	M(t) vs t plots
10.0	102	0.70	0.00	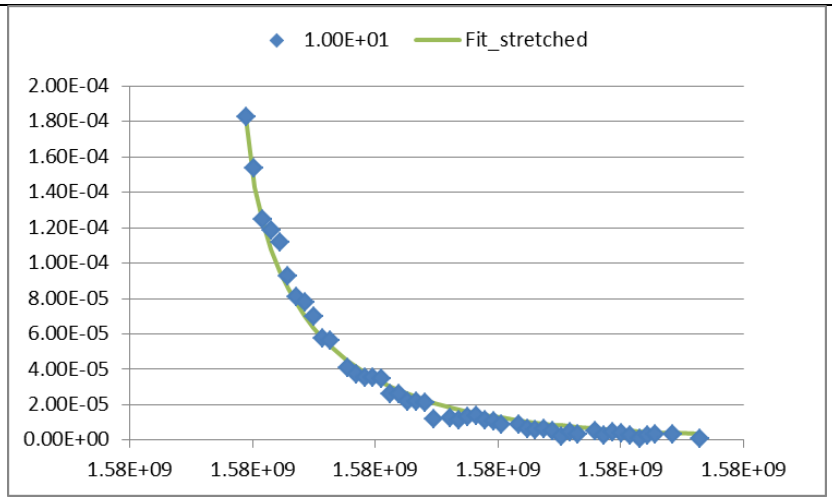
9.0	135	0.78	9.67E-7	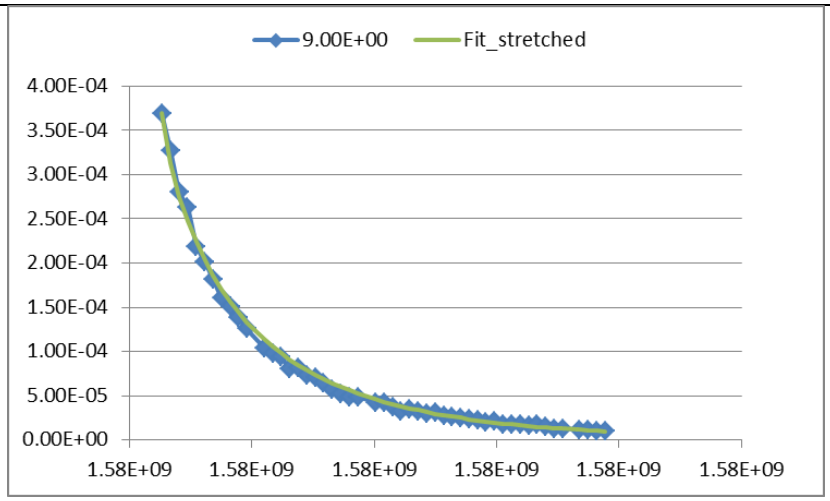

8.0	169.80	0.74	3.37E-6	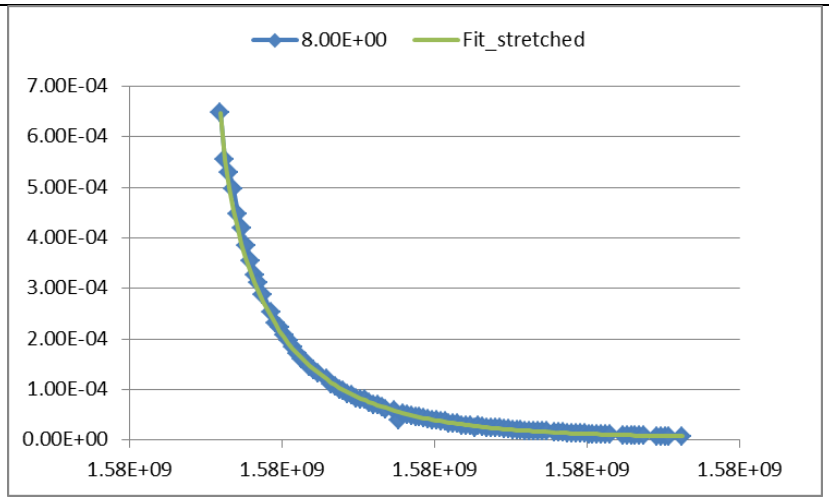
7.0	253.89	0.75	7.71E-6	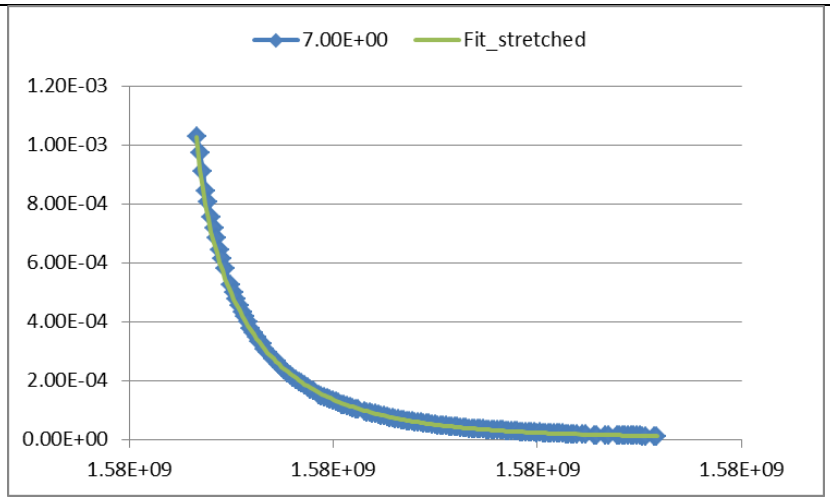
6.2	325.85	0.64	6.36E-7	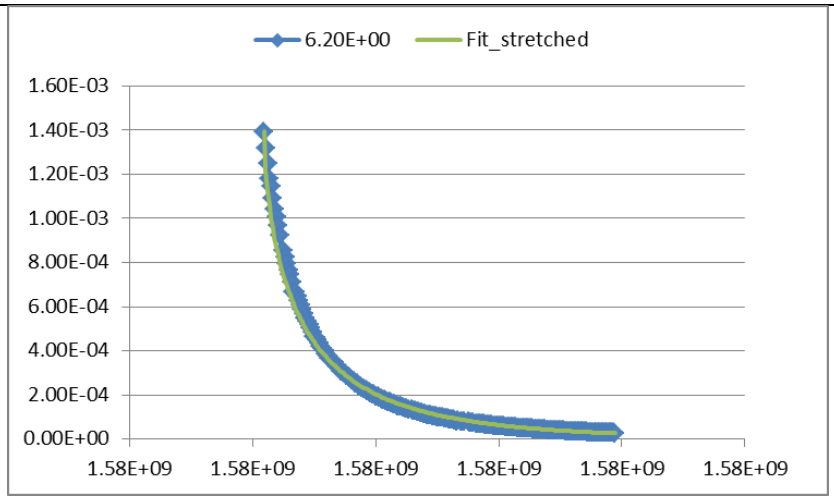

5.4	538.85	0.73	3.42E-5	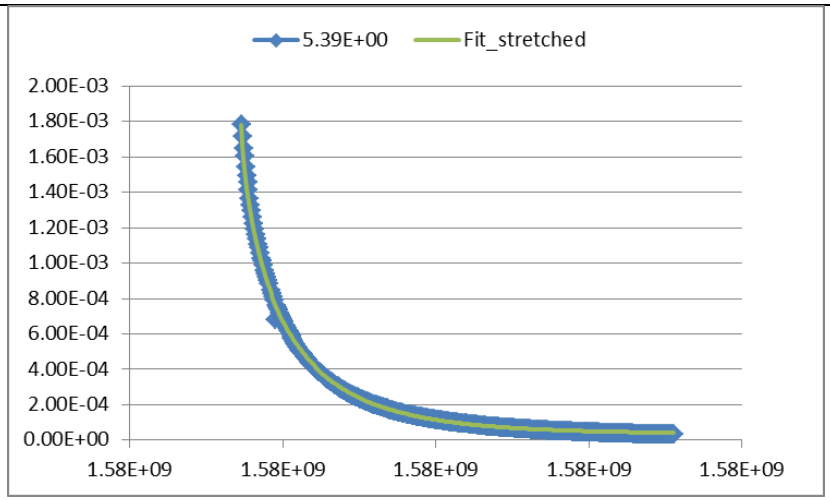
4.8	711.52	0.77	1.11E-4	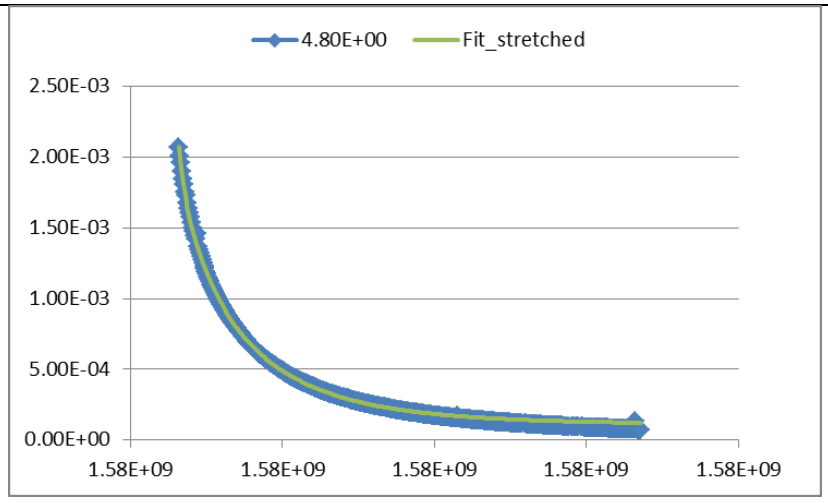

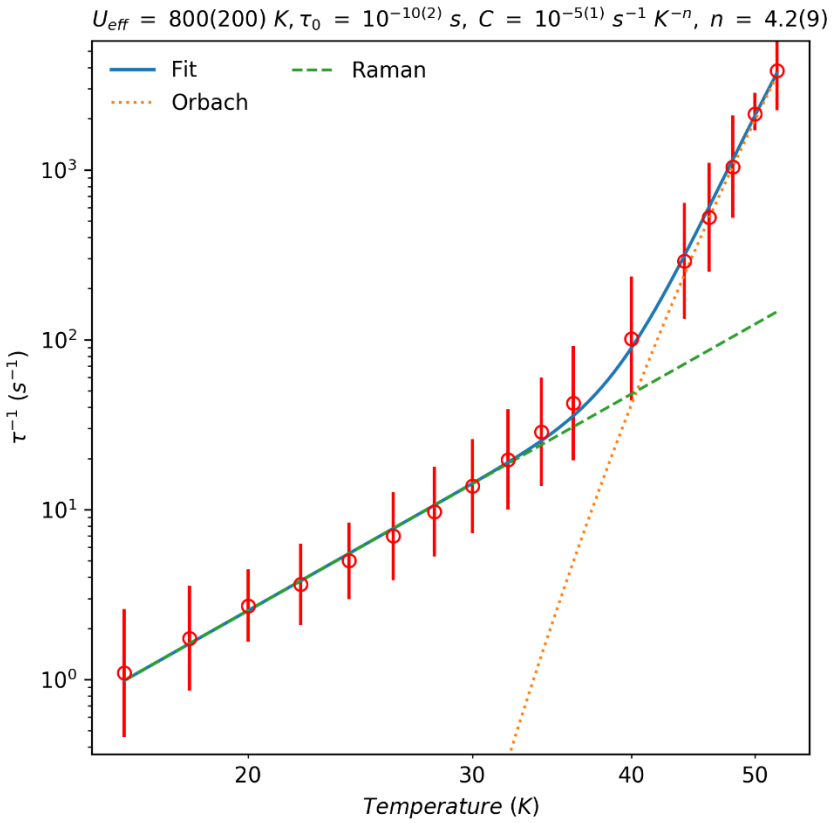

Figure S41. Temperature dependence of the magnetic relaxation rate of **[{Dy(Cp*)$_2$(μ-Me$_4$Al)}$_2$]**.

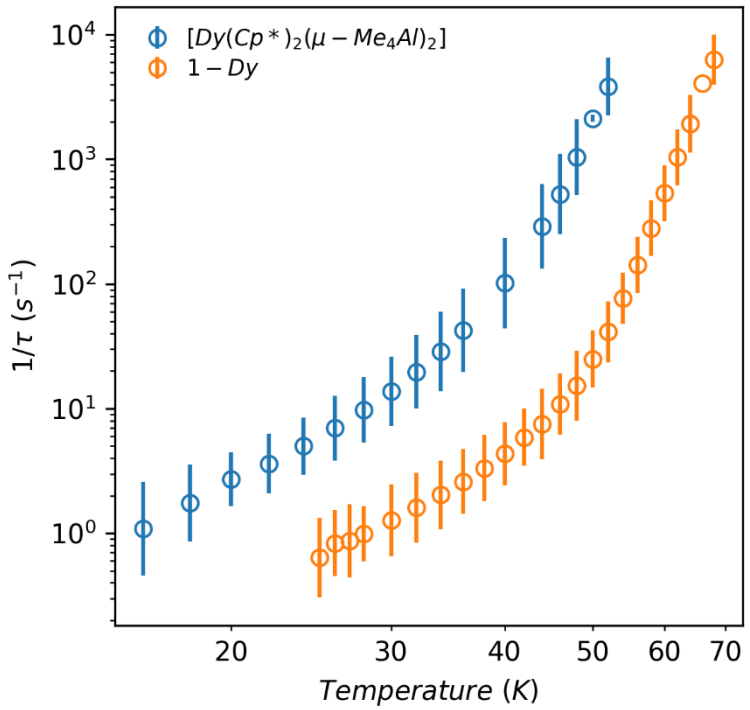

Figure S42. Comparison of the temperature dependence of the magnetic relaxation rate of **[{Dy(Cp*)$_2$(μ-Me$_4$Al)}$_2$]** and **1-Dy**.

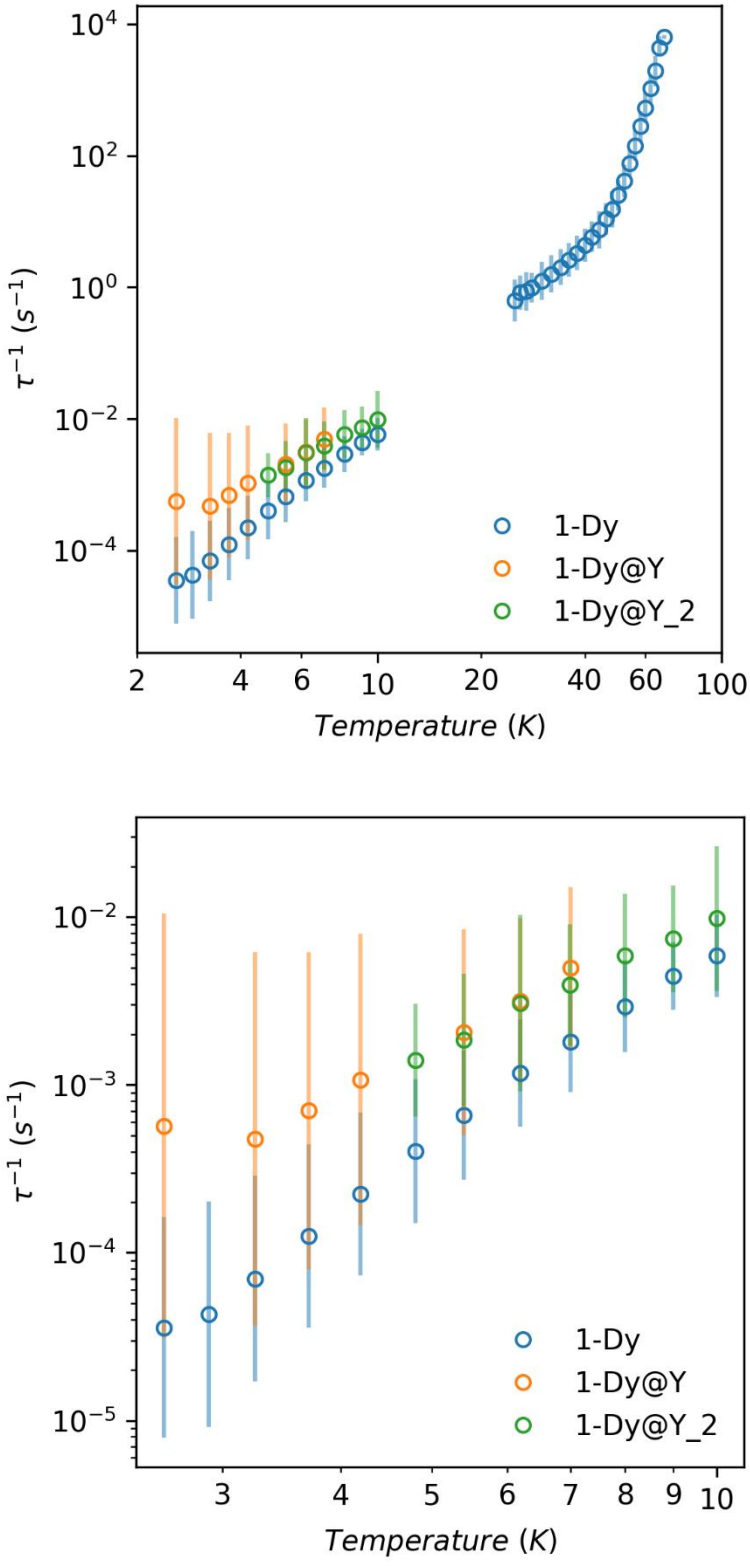

Figure S43. Temperature dependence of the magnetic relaxation rate of **1-Dy** (red), **1-Dy@Y** (blue) and **1-Dy@Y_2** (green) over the whole temperature range(top) and below 10 K (bottom).

7. CASSCF-SO electronic structure

We used MOLCAS 8.0[10] to perform CASSCF-SO calculations of the **[{Dy(Cp*)$_2$(μ-Me$_4$Al)}$_2$]** and **1-Dy** complexes in order to determine their electronic structures. We employed the molecular geometry of the metal-containing molecules from single crystal XRD structure with no optimisation, taking the largest disorder component only and substituting one dysprosium centre by yttrium. For **1-Dy**, we also run the calculation using lutetium, obtaining the same results within 0.5 cm^{-1}. Basis sets from the ANO-RCC library[11,12] were employed with VTZP quality for Dy atoms, VDZP quality for the cyclopentadienyl C atoms and VDZ quality for all remaining atoms, employing the second-order DKH transformation. Cholesky decomposition of the two-electron integrals with a threshold of 10^{-8} was performed to save disk space and reduce computational demand. The molecular orbitals (MOs) were optimized in state-averaged CAS(9,7)SCF calculations considering 21, 224 and 490 roots for the sextet, quartet and doublet spin states, respectively. These sets of spin-free states were then used to construct and diagonalise the spin-orbit coupling Hamiltonian in the basis of all sextet, 128 quartet and 130 doublets with the RASSI module. The crystal field decomposition of the ground J = 15/2 multiplet of the ^{6}H term was performed with the SINGLE_ANISO[13] module.

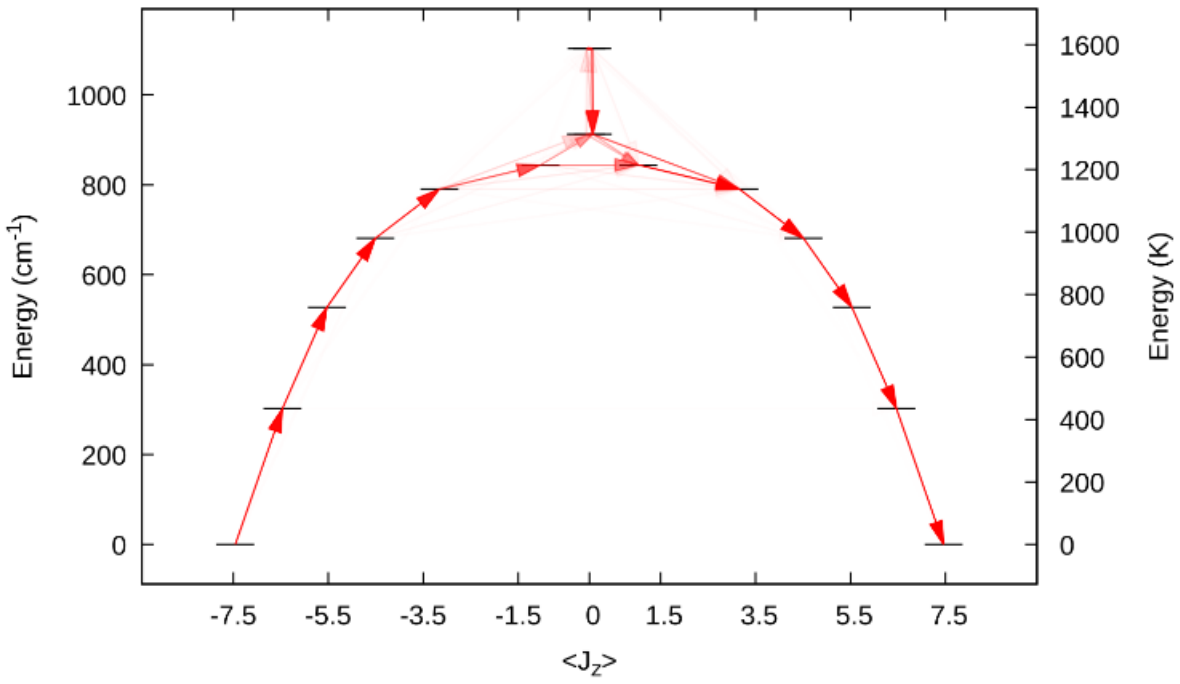

Fig. S44. Energy barrier to magnetic relaxation for a model of **1-Dy** containing one Dy^{3+} and one Lu^{3+} centre. Electronic states from CASSCF-SO calculations, labelled with their dominant m_J composition in the J = 15/2 basis. Arrows represent the Orbach relaxation pathway, where the opacity of the arrows is proportional to the transition probability approximated with the average matrix elements of magnetic moment connecting the states, $\gamma_{ij} = (1/3)[|\langle i|\mu_x|j\rangle|^2 + |\langle i|\mu_y|j\rangle|^2 + |\langle i|\mu_z|j\rangle|^2]$, normalised from each departing state and commencing from $|-15/2\rangle$.

Table S8. Electronic structure of the monomer of **[{Dy(Cp*)$_2$(μ-Me$_4$Al)}$_2$]** (one of the dysprosium centres has been substituted by yttrium) calculated with CASSCF-SO at the solid-state geometry, quantised along the g_3 direction of the ground doublet.

Energy (cm^{-1})	**Energy (K)**	g_1	g_2	g_3	**angle (deg)**	**Wavefunction**	$\langle J_z \rangle$
0.00	0.00	0.00	0.00	19.74	--	$97\%\|\pm 15/2\rangle + 3\%\|\pm 11/2\rangle$	$\pm$ 7.44
239.27	334.98	0.00	0.00	17.06	1.87	$98\%\|\pm 13/2\rangle + 2\%\|\pm 9/2\rangle$	$\pm$ 6.47
432.29	605.21	0.02	0.03	14.60	1.22	$97\%\|\pm 11/2\rangle + 3\%\|\pm 15/2\rangle$	$\pm$ 5.55
554.49	776.29	0.25	0.29	11.87	0.96	$98\%\|\pm 9/2\rangle + 2\%\|\pm 13/2\rangle$	$\pm$ 4.49
638.63	894.08	1.70	2.46	9.02	21.81	$85\%\|\pm 7/2\rangle + 9\%\|\pm 3/2\rangle$	$\pm$ 3.09
663.20	928.47	2.03	6.51	11.32	86.52	$29\%\|\pm 1/2\rangle + 26\%\|\pm 5/2\rangle + 12\%\|\mp 1/2\rangle + 11\%\|\mp 3/2\rangle + 11\%\|\mp 5/2\rangle$	$\pm$ 0.36
715.60	1001.83	1.34	3.49	11.47	89.87	$29\%\|\pm 3/2\rangle + 38\%\|\mp 5/2\rangle + 13\%\|\mp 3/2\rangle + 11\%\|\pm 5/2\rangle$	$\pm$ 0.34
896.25	1254.75	0.01	0,03	19.53	89.77	$26\%\|\pm 1/2\rangle + 26\%\|\mp 1/2\rangle + 18\%\|\pm 3/2\rangle + 16\%\|\mp 3/2\rangle$	$\pm$ 0.06

Table S9. Electronic structure of the monomer of **1-Dy** (one of the dysprosium centres has been substituted by lutetium) calculated with CASSCF-SO at the solid-state geometry, quantised along the g_3 direction of the ground doublet.

Energy (cm^{-1})	**Energy (K)**	g_1	g_2	g_3	**angle (deg)**	**Wavefunction**	$<J_z>$
0.00	0.00	0.00	0.00	19.80	--	$98\%\|\pm 15/2\rangle + 2\%\|\pm 11/2\rangle$	$\pm$ 7.47
298.38	429.28	0.00	0.00	17.05	0.87	$99\%\|\pm 13/2\rangle + 1\%\|\pm 9/2\rangle$	$\pm$ 6.47
526.66	757.70	0.00	0.01	14.50	0.88	$98\%\|\pm 11/2\rangle + 2\%\|\pm 15/2\rangle$	$\pm$ 5.53
681.19	980.02	0.14	0.14	11.83	2.01	$98\%\|\pm 9/2\rangle + 1\%\|\pm 13/2\rangle$	$\pm$ 4.51
790.28	1136.97	1.68	2.48	8.54	4.26	$89\%\|\pm 7/2\rangle + 8\%\|\pm 3/2\rangle$	$\pm$ 3.22
841.62	1210.84	2.95	7.16	9.81	89.34	$47\%\|\pm 5/2\rangle + 32\%\|\pm 1/2\rangle + 10\%\|\mp 3/2\rangle + 5\%\|\mp 7/2\rangle$	$\pm$ 0.95
908.48	1307.03	0.38	1.19	14.99	89.40	$47\%\|\pm 3/2\rangle + 36\%\|\mp 5/2\rangle + 10\%\|\mp 1/2\rangle + 4\%\|\pm 7/2\rangle$	$\pm$ 0.13
1104.14	1588.52	0.03	0.04	19.43	89.45	$53\%\|\pm 1/2\rangle + 33\%\|\pm 3/2\rangle + 10\%\|\mp 5/2\rangle$	$\pm$ 0.05

Table S10. Electronic structure of the monomer of **1-Dy** (one of the dysprosium centres has been substituted by yttrium) calculated with CASSCF-SO at the solid-state geometry, quantised along the g_3 direction of the ground doublet.

Energy (cm^{-1})	**Energy (K)**	g_1	g_2	g_3	**angle (deg)**	**Wavefunction**	$<J_z>$
0.00	0.00	0.00	0.00	19.80	--	$98\%\|\pm 15/2\rangle + 2\%\|\pm 11/2\rangle$	$\pm$ 7.47
298.20	429.04	0.00	0.00	17.05	0.87	$99\%\|\pm 13/2\rangle + 1\%\|\pm 9/2\rangle$	$\pm$ 6.47
526.38	757.34	0.00	0.01	14.50	0.88	$98\%\|\pm 11/2\rangle + 2\%\|\pm 15/2\rangle$	$\pm$ 5.53
680.81	979.53	0.14	0.14	11.83	2.02	$98\%\|\pm 9/2\rangle + 1\%\|\pm 13/2\rangle$	$\pm$ 4.51
789.80	1136.34	1.68	2.49	8.54	4.27	$89\%\|\pm 7/2\rangle + 8\%\|\pm 3/2\rangle$	$\pm$ 3.21
841.05	1210.08	2.95	7.16	9.81	89.33	$46\%\|\pm 5/2\rangle + 31\%\|\pm 1/2\rangle +$ $10\%\|\mp 3/2\rangle + 5\%\|\mp 7/2\rangle$	$\pm$ 0.92
907.89	1306.24	0.39	1.20	14.99	89.40	$48\%\|\pm 3/2\rangle + 37\%\|\mp 5/2\rangle +$ $10\%\|\mp 1/2\rangle + 4\%\|\pm 7/2\rangle$	$\pm$ 0.14
1103.51	1587.70	0.03	0.04	19.43	89.45	$40\%\|\pm 1/2\rangle + 27\%\|\mp 3/2\rangle +$ $14\%\|\mp 1/2\rangle + 7\%\|\mp 5/2\rangle$	$\pm$ 0.11

In order to explain why **1-Dy@Y** relaxes faster than **1-Dy** (Figure S42 and middle and bottom rows of Figure S27), we calculate the interaction between the two magnetic centres assuming that the dipolar coupling is the leading term, and it is described as:

$$\boldsymbol{J^{dip}} = \frac{\mu_B^2}{R^3}\left[\boldsymbol{g_1}\cdot\boldsymbol{g_2} - 3\frac{(\boldsymbol{g_1}\cdot\mathbf{R})(\mathbf{R}\cdot\boldsymbol{g_2})}{|R|^2}\right]$$

Due to the existence of an inversion centre in the molecule, $\boldsymbol{g_1}$ and $\boldsymbol{g_2}$ tensors are co-parallel and one can ignore their relative orientations. Using $\boldsymbol{g_1} = \boldsymbol{g_2} = (0.00, 0.00, 19.80)$ (Table S9) and $\mathbf{R} = (-7.33, -0.65, 0.17)$ (from XRD data in the same reference frame as $\boldsymbol{g_1}$ and $\boldsymbol{g_2}$), $J_{zz}^{dip} = -0.21\ cm^{-1}$ in the $\hat{H} = -2J_{zz}^{dip}\hat{S}_{z,1}\hat{S}_{z,2}$ formalism, resulting in a 0.42 cm^{-1} gap at zero field. The external magnetic

field required to induce a Zeeman splitting of the same value, leading to a degeneracy of the states and therefore a fast quantum tunnelling of magnetisation, can be approximated to 0.09 T using $E = \mu_B g B_{ext} m_S$, with |E| = 0.42 cm^{-1}, $g = 19.8$ and $m_S = 1/2$. This value of 0.09 T matches very well the field position where **1-Dy** starts to lose magnetisation sharply, in contrast with **1-Dy@Y** (Figure S27) which is far closer to zero-field (indeed, **1-Dy** loses *ca.* 28% magnetisation between 0.1 T and 0.05 T while **1-Dy@Y** loses only *ca.* 8%). Thus, the energy offset imposed by dipolar interactions in **1-Dy** in the absence of applied field (conditions used to measure relaxation times), penalises QTM processes and results in slower dynamics than **1-Dy@Y**, where the ground Kramers doublet is degenerate in zero-field.

8. References

1. (a) M. A. Busch, R. Harlow and P. L. Watson, *Inorg. Chim. Acta*, 1987, **140**, 15; (b) P. L. Watson and T. Herskovitz, *Am. Chem. Soc. Symp. Ser*., 1983, **212**, 459; (c) P. L. Watson, *J. Am. Chem. Soc*., 1983, **105**, 6491.

2. P. Evans, D. Reta, G. F. S. Whitehead, N. F. Chilton and D. P. Mills, *J. Am. Chem. Soc*., 2019, **141**, 19935.

3. *CrysAlisPRO*, version 39.27b; Oxford Diffraction /Agilent Technologies UK Ltd: Yarnton, U.K., 2017.

4. G. M. Sheldrick, *Acta Crystallogr., Sect. A*., 2008, **64**, 112.

5. G. M. Sheldrick, *Acta Crystallogr., Sect. C*, 2015, **71**, 3.

6. O. V. Dolomanov, L. J. Bourhis, R. J. Gildea, J. A. K. Howard and H. Puschmann, *J. Appl. Crystallogr*., 2009, **42**, 339.

7. L. J. Farrugia, *J. Appl. Crystallogr*., 2012, **45**, 849.

8. *POV-Ray. Persistence of Vision Raytracer*; Persistence of Vision Pty. Ltd.: Williamstown, Victoria, Australia, 2013.

9. G. A. Bain and J. F. Berry, *J. Chem. Ed*., 2008, **85**, 532.

10. F. Aquilante, J. Autschbach, R. K. Carlson, L. F. Chibotaru, M. G. Delcey, L. De Vico, I. Fernandez Galván, N. Ferré, L. M. Frutos, L. Gagliardi, M. Garavelli, A. Giussani, C. E. Hoyer, G. Manni, H. Lischka, D. Ma, P. Å. Malmqvist, T. Müller, A. Nenov, M. Olivucci, T. B. Pedersen, D. Peng, F. Plasser, B. Pritchard, M. Reiher, I. Rivalta, I. Schapiro, J. Segarra-Martí, M. Stenrup, D. G. Truhlar, L. Ungur, A. Valentini, S. Vancoillie, V. Veryazov, V. P. Vysotskiy, O. Weingart, F. Zapata and R. Lindh, *J. Comput. Chem*., 2016, **37**, 506.

11. B. O. Roos, R. Lindh, P.-Å. Malmqvist, V. Veryazov and P.-O. Widmark, *J. Phys. Chem. A*., 2004, **108**, 2851.

12. B. O. Roos, R. Lindh, P.-Å. Malmqvist, V. Veryazov and P.-O. Widmark, *J. Phys. Chem. A*., 2005, **109**, 6575.

13. L. Ungur and L. F. Chibotaru, *Chem. Eur. J*., 2017, **23**, 3708.